REVISION 2

Computational study of the elastic behaviour of the $2M_1$ Muscovite-Paragonite series

NOEMÍ HERNÁNDEZ-HARO,[1] JOAQUÍN ORTEGA-CASTRO,[2] CARLOS PÉREZ DEL VALLE,[3] DANIEL MUÑOZ-SANTIBURCIO,[1] CLARO IGNACIO SAINZ-DÍAZ,[1] AND ALFONSO HERNÁNDEZ-LAGUNA[1,*]

[1] Instituto Andaluz de Ciencias de la Tierra. CSIC-UGR, Av. de las Palmeras 4, 18100-Armilla, Granada, Spain.

[2] Departamento de Química. Universidad de las Islas Baleares. 07122, Palma de Mallorca, Spain.

[3] DCM-Université Joseph Fourier-Grenoble I, 38041 Grenoble Cedex 9, France.

Abstract Elastic properties are an important issue in explaining the behaviour of seisms and to ascertain the mineralogical composition of the Earth's shells through which seismic waves pass. Computational methods can yield an additional, detailed, free-of-heterogeneity model knowledge of the mineral series of interest. Therefore, a computational study on the influence of the interlayer cation in the muscovite-paragonite (Ms-Pg) series on the crystal cell, internal geometry, and the elastic properties was made to shed light on the mineralogical, geophysical, and geochemical properties of the series. These properties have been calculated by means of Density Functional Theory (SIESTA2.0.2 code). The crystal structure and internal geometry agreed with the range of experimental values in the literature. In general, elastic stiffness constants (EC) agreed with the known experimental values. ECs of different interlayer cation configurations for the middle concentration sample showed very similar values, except for C_{33}, The majority of ECs, with the exception of C_{33} and C_{66}, decreased as a function of Na* [Na/(Na+K)], many of which showed ideal crystalline solution behaviour, and some showed mixing terms. The polycrystalline bulk modulus registered similar values for the end members of the series and a minimum at Na*=0.5, although an estimate of the value at room temperature made the Pg stiffer than Ms; while the shear modulus showed a decreasing trend as a function of

the Na^{*}. Velocities of the sound waves lowered as a function of Na*. Local deformabilities were also studied, where the highest deformability was found for the interlayer space. The results are discussed in the framework of the mineralogical, geochemical, and geophysical knowledge of the series.

Keywords Muscovite-paragonite series, crystal structure, local geometries, elastic-stiffness constants, bulk and shear moduli, local deformabilities, DFT calculations.

INTRODUCTION

In seisms, the velocities of the acoustic waves are functions of the elastic properties of the materials they pass through, and from these two parameters it is possible to account for the structure, compositions and dynamics of the Earth's shells. Thus, although the elastic properties of minerals are key geophysical data, it is frequently difficult to measure the exact elastic-stiffness constants (ECs), especially in natural minerals where cation order/disorder, morphological, crystal-chemical, and crystal-physical heterogeneities exist (Mondol et al., 2008). However, computational methods can yield reliable crystal structures and ECs free of these natural heterogeneities (Karki et al. 2001; Stixrude 2002; Stixrude and Peacor 2002; Weirich (2004), Ortega-Castro et al. 2010; and Millizer et al. 2011). This would help explain the crystal-chemical, crystal-physical, mineralogical, and petrological behaviour of minerals and aid interpretations of the seismologic data.

Phyllosilicates, found in the Earth's crust and even in the upper mantle, are also found in subduction slabs in a wide compositional range, depending on the pressure (P), temperature (T), and composition of the bulk rock. Micas are 2:1 phyllosilicates (21P) (Moore and Reynold, 1989), and because of many different cation substitutions form a major group of minerals. Micas are also one of the sources of water in the deep subduction zones.

Because of their high chemical stability, micas have major industrial applications and include properties of films measuring several microns. Elastic, tough, and thermally resistant, micas have high dielectric strength, so that they are valuable in industries related to optics and electricity. Micas show a wide compositional formula, which allows the gradation of some of their properties depending on the composition.

Muscovite (Ms) [$KAl_2(Si_3Al)O_{10}(OH)_2$] is a dioctahedral mica, one of the most common and abundant minerals in metamorphic rocks (metapelites, shales, micaschists, gneiss, metabasites, etc.) and considered an useful petrogenetic indicator (Comodi and Zanazzi, 1997). Ms is an end member of the Ms-paragonite solvus. Paragonite (Pg) is the ideal end member of the series with Na^+ instead of K^+ as an interlayer cation. This series has substitutions on the octahedral (Oc or VI) sheet, particularly Ms, which can undergo the substitution of Fe^{3+}, Fe^{2+} and Mg^{2+}, yielding celadonite and phengite series; in addition, different Al^{3+} substitutions also take place on the tetrahedral (T or IV) sheet. Phengitic Ms

are stable at very high pressures in mature subduction zones, and they may be an important factor in the mass transfer of K (Peacock et al. 1994; Domanik and Holloway 1996). The Ms-Pg solvus changes the interlayer cations in contact with hydrothelmal solutions of (Na,K)Cl, the Pg being less stable than Ms (Iiyama, 1964, Pascal and Roux, 1985). The Ms-Pg series was studied to be used as a geothermometer and a geobarometer (Guidotti et al, 1994; Blencoe et al. 1994). The effect of the Oc and interlayer cation substitutions on the crystal structure of this series was studied by Guidotti et al. (1992) (GEA92), highlighting an important lack of miscibility at the middle range of the solvus.

Ms was the first 21P to have its ECs measured. Aleksandrov and Ryzhova (1961), by means of ultrasonic measurements, provided 9 of the 13 ECs. Employing Brillouin scattering spectrometry, Vaughan and Guggenheim (1986) and McNeil and Grimsditch (1993) measured the 13 independent ECs of Ms. These authors found that Ms shows relatively little anisotropy along the *ab* basal plane and is much more anisotropic in planes where the *c* axis is included. By means of empirical interatomic potentials, Collins et al. (1992) calculated the ECs of Ms, and their pure normal and shear ECs being higher than the previous experimental values. Militzer et al. (2011) calculated the ECs and sound velocities of Ms, illite-smectite, kaolinite, dickite, and nacrite by using plane-wave methods in order to interpret the anisotropy of shales.

In the Ms-Pg series, a study of the crystal structure, elastic properties, and internal geometry changes as a function of the interlayer cations can help to interpret the mineralogical, geochemical, and geophysical behaviour of this series without natural heterogeneity. The suitability of this study was highlighted by Militzer et al. (2011): "…Other potentially important effects to be investigated included the role of intra-layer cation radius (e.g. Na substitution for K)…The elastic properties of naturally occurring clays depend on the degree and type of isomorphic substitution and interlayer cations, since it controls the strength of interlayer bonding…..". In addition, the detailed knowledge of the internal geometry, crystal structure, and elastic properties of series can shed light on many aspects of such behaviour as geothermometer, geobarometer, and geochemical reactions.

The present work has the following aims: i) to determine the crystal structure and internal geometry as a function of the interlayer cations; ii) to ascertain the ECs as a function of the interlayer cations; iii) to elucidate how order/disorder of interlayer cations

can influence the ECs; and iv) to explain how the internal groups are deformed as a function of the normal strains and the interlayer cations.

METHODS

Computational methods

SIESTA2.0.2 code (Sánchez-Portal et al. 1997; and Artacho et al. 1999; Soler et al., 2005) has been used to calculate the electron density of the structure of the series by means of Density Functional Theory (Hohenberg and Kohn 1964; Kohn and Sham 1965). Both the internal geometry and the cell parameters have been optimized in the same run, by using an algorithm based on the Broyden method. Generalized gradient approximation (GGA) with the Perdew-Burke-Ernzerhof (1996) (PBE) correlation-exchange functional was used, and one local density approximation (LDA) calculation on Ms has been also performed with the Ceperley-Alder exchange-correlation functional (Ceperley and Alder 1980). A mesh cut-off of 500 Ry and 15 and 9 *k*-points in the Monkhorst Pack grid were found to be adequate to offer a high level of convergence in the 84 and 168 atoms cells, respectively. Troullier-Martins norm-conserving pseudopotentials (Troullier and Martins 1991) were used. The convergence threshold of forces and stresses were 0.005 eV/Å and 0.002 GPa, respectively. All calculations were performed at a pressure of 0 GPa.

Our calculations were performed with numerical atomic orbitals, and double-ζ plus polarization basis sets. The pseudopotentials and basis sets used in this work were previously optimised for a set of dioctahedral 2:1 phyllosilicates (Ortega-Castro et al. 2008, 2009). In a previous paper (Ortega-Castro et al. 2010), the high-pressure behaviour of Ms was calculated in both the local density approximation (LDA) with the Ceperley-Alder exchange-correlation functional (Ceperley and Alder 1980) and GGA-PBE approach, finding that the GGA yielded cell parameters closer to the experimental data than did LDA. In addition, White et al. (2009) demonstrated that GGA functional showed lower energies and more accurate geometries.

Elastic equations

ECs were calculated via the generalized Hooke's law, expressed by the following tensor equation:

$$\sigma_{ij} = C_{ijkl}\varepsilon_{kl} \qquad \forall i,j,k,l = 1,2,3 \equiv x,y,z \tag{1}$$

Where σ_{ij} and ε_{kl} stand for the *ij* and *kl* terms of the stress and strain tensors, respectively, and C_{ijkl} stands for the *ijkl* term of the EC tensor. This equation can be simplified in Voigt notation $\sigma_p = C_{pq}\varepsilon_q$ (Nye, 1957). Our calculated ECs will be given in this last notation.

We employed the finite-strain method (Gale et al. 2001, Milman and Warren 2001; Karki et al. 1997a, b; Adams and Oganov 2006; Oganov et al. 2001). ECs were calculated using strains of ±0.03 and ±0.02, with the exception of C_{33}, which was calculated with strains of ±0.005. This last reduction in the strain came from the reduction of the linearity between the stress and strain for the normal EC associated with the *c* axis. ECs showed an error < 2.2 GPa, with the exception of C_{33} of the samples of $Na^* = Na^+/(Na^+ + K^+) = 0.25$ and 0.50, with an error < 3.7 GPa. No thermal or pressure effects were included in the calculations.

The bulk and shear moduli were calculated from the EC tensors with the Hashin and Shtrikman bounds (Hashin et al. 1962a, b), with the Watt and Peselnick (1980), and Watt (1979, 1980, 1987) methods. The average of both bounds could be considered a reliable value of the polycrystalline aggregate (Hill 1952).

The bond distances and other internal geometric deformations were calculated as:

$$\delta^i_{jj} = \frac{l^i{}_{\varepsilon_{jj}} - l^i{}_0}{l^i{}_0} \tag{2}$$

where $l^i{}_{\varepsilon jj}$ is the *i* bond length, or average of internal distances or angles of one atomic group, when the crystal undergoes a particular normal strain (ε_{jj}) and $l^i{}_0$ is the non-strained bond length. These were studied as a function of the normal strains as

$$\delta^i_{jj} = f(\varepsilon_{jj}) \tag{3}$$

We define the deformability of the *i* geometrical parameter as

$$D^i_{jj} = \frac{\partial \delta^i_{jj}}{\partial \varepsilon_{jj}} \tag{4}$$

where δ^i_{jj} was fitted to a linear function of the different ε_{jj}'s by the least-squares method. The deformabilities could be considered a suitable way to analyse the internal deformations and the bonding of the crystal.

Crystalline Solutions

An important issue when seeking to rationalize the physical quantities with the chemical composition in crystalline solutions arises by the ideal additive mixing law, that for the crystal cell volume can be written as $V = \sum_j X_j V_j$, where V is the volume of any member of a crystalline solution, with a composition described by the molar fraction, X_j, with respect to the j-end-members of the crystalline solutions, with volume V_j . In the case of two components, a variable reduction to determine a single variable can be used to formulate a linear equation ($V = A_0 + A_1 X_2$). The separation of the ideal addition law, for a binary crystalline solution with the variable reduction, may also be written in the form of a polynomial equation (Waldbaum and Thompson 1968, $V = \sum_{i=0}^{3} A_i X_2^i$). This equation can be rearranged in an ideal addition law plus a mixing term, which, for the case of symmetrical crystalline solution form (A_3=0), can be written:

$$V = (\sum_{i=0}^{2} A_i) X_2 + A_0(1 - X_2) - A_2 X_2 (1 - X_2) \qquad (5)$$

where the coefficient of the first term of the second member corresponds to the volume of the crystalline solution of the independent variable end-member; the second coefficient corresponds to the volume at the other end-member in the crystalline solution; and the last term is considered a mixing term, ΔV_{mix} , which explains the excess of volume out of the ideal solution. If $A_3 \neq 0$ the equation is written as:

$$V = \left(\sum_{i=0}^{3} A_i \right) X_2 + A_0(1 - X_2) - (A_2 + A_3) X_2 (1 - X_2)^2 - (A_2 + 2A_3) X_2^2 (1 - X_2) \quad (6)$$

The two first terms have the same meaning as before, and the last terms are the asymmetrical mixing terms, where the coefficient of the first may be interpreted as the volume excess of the independent variable end-member, and the second one as the volume

193 excess of the other end-member in the binary crystalline solution. Both of them are equal to
194 the Margules parameters (Waldbaum and Thompson 1968). All terms depend on pressure
195 and temperature.

196 For the case of cell parameters a similar ideal crystalline solution law is given by the
197 Vegard's law ($a = \sum_j X_j a_j$), where a is the cell axis of the any member of a solid solution,
198 with a composition described by the molar fraction, X_j, with respect to the j-end-members
199 of the crystalline solutions with a_j axes. Separation of the Vegard's law for the crystal
200 parameters could be described by mixing terms similar to Eqs. (5) and (6).

201 The ECs of a solid solution should follow similar ideal crystalline solution laws
202 (Isaak and Graham 1976, and Babuska et al. 1978) such as:

203 $$(C_{pq}) = \sum_k X_k (C_{pq})^k \qquad (7)$$

204 where (C_{pq}) is the pq EC of the any member of the solid solution and $(C_{pq})^k$'s are the pq k-
205 end-member ECs of the series. Deviation from this approach could be also approached with
206 a mixing terms similar to Eqs. (5) and (6). If the additive law for volume is differentiated
207 with respect to pressure, and considering, in an initial approach, that the mixing terms are
208 not dependent on pressure, a similar additive law also results (Takahashi et al. 1970):

209 $$\frac{V}{B} = \sum_j X_j \frac{V_j}{B_j} \qquad (8)$$

210 where B and V are the bulk modulus and the volume of crystal cell of any member of a
211 solid solution, while the X_j's represent the end-member molar fractions variables, with V_j
212 and B_j end-member values. Deviation of this law might also be approached by mixing
213 terms. Similar expressions for the ECs can be used to analyse these properties (Babuska et
214 al. 1978). As Babuska et al. (1978) recommended, the simplest law must be used (Eq. 7) to
215 describe the systems, but when Eq. 7 is not sufficient to systematize the system, an
216 equation similar to Eq. 8 can be also used:

217 $$\frac{V}{C_{pq}} = \sum_j X_j \frac{V_j}{C^j_{pq}} \qquad (9)$$

218

219 **Crystal models**

220

The $2M_1$ Ms-Pg series model consists of a layered structure with different sheets (Fig. 1a):

i) The T-sheet is composed of SiO_4 tetrahedral units, which are joined by three oxygens in a tetrahedron base (the so-called basal oxygens), forming quasi-hexagonal rings. The remaining oxygens of the SiO_4 units, which are perpendicular to the basal plane, are the so-called apical oxygens. Some Si^{4+} cations may be replaced by Al^{3+}.

ii) The Oc-sheet is composed of aluminium oxy-hydroxide octahedra. All the apical oxygens of the T-sheet are shared with the Oc-sheet, and two oxygens of the octahedron are saturated with hydrogens. In the Oc-sheet, only two-thirds of the octahedra have their centres occupied with Al^{3+} (dioctahedral phyllosilicate series).

iii) In Ms-Pg series, two T-sheets and one Oc-sheet form T-Oc-T layers, belonging to the 21P series. The tetrahedra must rotate in order to fit both sheets properly. This fitting changes the hexagonal symmetry of the T sheet to a ditrigonal symmetry. This rotation is defined by the α angle. Crystal chemistry, pressure, and temperature affect the α angle (Comodi and Zanazzi 1997, Mercier et al. 2006, Ortega-Castro et al. 2010).

iv) Interlayer spaces occur between the T-Oc-T layers. The charge imbalance caused by isomorphic cation substitution in the tetrahedral sheet is compensated for by cations located in the interlayer space, such as K^+ and Na^+. Different proportions of these cations occur in the Ms-Pg series. Interlayer cations are bonded to the layers by electrostatic forces, the distances of bonds are the largest in the structure, and the density of bonds is the smallest in the structure, so that the forces between the layers are the weakest in the structure (Fig. 1a) and responsible for the main chemical and physical properties of phyllosilicates.

v) The different stacks of the T-Oc-T sheets produce polytypism, the $2M_1$ being the most frequent polytype in this series (Fig. 1a), although the 3T stacking is also found, and other more scarce polytypes are also described. The crystal structure in our series was of $2M_1$ polytype (Fig. 1a).

vi) The structural formula of the Ms-Pg series is $[K_{1-x}\ Na_x\ Al_2(Si_3Al)O_{10}(OH)_2]$. We have calculated the elastic properties of five members of the series: Ms (x = 0), three intermediates with different concentrations of K^+ and Na^+ (x = 0.25, 0.50, and 0.75) and Pg (x = 1). Calculations for x = 0, 0.5, and 1 were performed with 1×1×2 supercells (84

atoms/supercell, Fig. 1a); while for x = 0.25 and 0.75 larger cells were needed, so 1×2×2 supercells (168 atoms per supercell) were built. All systems are given in the input file as a single unit cell.

vii) In our $2M_1$ model, two interlayer spaces are included (Fig. 1a). For the x = 0.50 compound different interlayer cation configurations are studied. The interlayer cation configuration in Figure 1a is called **c0**.

RESULTS AND DISCUSSIONS

Structure

1. Crystal structure. Table 1 provides structural information on the calculated unit cells, comparing them with the known experimental data of Ms and Pg. By plotting the *a* cell parameter as a function of Na^* [Na/(Na+K)] (Fig. 2a), a general quadratic behaviour was found, showing a symmetric mixing term, smaller than the symmetric mixing term of GET92 (0.1 Å). However, from the data of Flux and Chatterjee (1986) and Roux and Hovis (1996), we calculated the asymmetric mixing terms by fitting to a cubic equation (0.009 due to the parameter excess of Ms and -0.021 due to Pg, and 0.002 due to Ms and +0.066 Å due to Pg, respectively) slightly different from those resulting from our data (0.08 and -0.01 due to Ms and Pg excess, respectively). Values in the work by Flux and Chatterjee (1986), GEA92 (up to Na*=0.3), Roux and Hovis (1996), and other authors are included in Figure 2a. Our values closely parallel those of the Flux and Chatterjee (1986), GEA92, and Roux and Hovis (1996) values and are between the values of the other experimental values included in Figure 2a. GEA92 found *a* = 5.186 Å (average value of 5.187 Å) for Ms, which agrees with our calculated value of 5.187 Å. Although the GEA92 samples in Figure 2a had no octahedral substitutions, most of the different authors' samples showed octahedral substitutions, which can influence the cell parameters. The *b* axis as a function of Na^* (Fig. 2b) showed a similar behaviour to that of *a*, with a higher quadratic coefficient. Therefore, the mixing of both cations exerted stronger effects on the *b* than on the *a* axis. Our symmetric mixing term (0.08 Å) was similar to the GEA92 term (0.0515 Å) and to the Flux and Chatterjee (1986) term (0.044 Å). However, Roux and Hovis (1996) found

asymmetric mixing terms when a cubic polynomial was fitted to their data (-0.142 for the parameter excess of Ms and 0.20 Å for Pg), slightly different from ours parameter excess (+0.06 for Ms and 0.12 Å for Pg). The b = 9.006 Å of Ms was consistent with the values found by GEA92 (8.991 Å, and 8.992 Å for the average). These authors did not provide any values or functions for a and b for Pg's. Eugster et al. (1972), in 1M polytypes, gave the ab in Å^2 as a function of Na*, finding a symmetric term very close to our term (0.83 and 0.73 Å^2, respectively). The parameter $½csin\beta$ showed a clearly linear behaviour (Fig. 2c), where our slope was of the same order as the linear coefficient of the Ms' of GEA92. However, GEA92, Flux and Chatterjee (1986) and Roux and Hovis (1996) found symmetric mixing terms. The experimental $½csin\beta$ values for the Ms and Pg end-members of the series were, respectively, 10.027 Å and 9.610 Å, and our calculated values were 10.028 Å and 9.533 Å (deviation of 0.8%), respectively. Although Ms computational values were identical to GEA92's values, the increased Na* values were higher than ours (Fig. 2b). Computational values were between different authors' values in the region of Ms'. In this cell parameter, the weak interactions of the interlayer space were included, and these interactions were determinant for the values of $½csin\beta$, so that the approach used overestimated the electron density in the interlayer space when Na* increased. The volume of the cell as a function of Na* (Fig 2c) showed a net quadratic behaviour with a downward concavity, which led to a symmetric mixing term of ΔV_{mix} = 14.7 Å^3 close to the Flux and Chatterjee (1986), and Roux and Hovis (1996) symmetric mixing term (15.8; and 30.0 Å^3, respectively) . Eugster et al (1972), for 1M polytypes, gave two fittings for the volume: i) with a symmetric mixing volume [26.15 Å^3 (extrapolated to the equivalent volume of the $2M_1$ polytype)]; and ii) with asymmetric mixing terms [34.99 due to the Ms and 22.84 Å^3 for the Pg excess of volume (extrapolated to the equivalent volume of the $2M_1$ polytype)]. In general, the mixing behaviour is similar to that calculated from the literature. Clearly, the mixing term on the volume came from the effects of the substitution on the ab plane. Because of the positive sign of the ΔV_{mix}, in an increasing pressure system, any member of the solid solution would migrate to K-richer compositions (GEA92, and Guidotti et al. 1998). The average values of GEA92 for the Ms and Pg samples were 935.0 and 876.8 Å^3, respectively, and our values were 937.0 and 868.8 Å^3

(deviation of 0.2% and 0.9%, respectively). LDA parameters showed larger deviations, especially those concerning to $\frac{1}{2}csin\beta$ and volume (4% and 7%, respectively).

The linear function slope of $\frac{1}{2}csin\beta$ as a function of Na^* was 17-fold larger than *a* and *b* slopes, indicating the great anisotropy of these minerals, the importance of the layer stacking, and the effect of the cations in the interlayer space. In addition, the effective cationic Na^+ radius (for a coordination number of 12, r = 1.39 Å, Shannon, 1976) is smaller than that of K^+ (r = 1.64 Å, Shannon, 1976), hence the increase of the $r(Na^+)/r(K^+)$ ratio affects the *c* axis, in a stronger way than the *a* and *b* axis. Therefore, the crystal-chemistry behaviour of the series was similar to the experimental behaviour (GEA92). The computational situation could be considered to be a model behaviour for the series, free of cationic heterogeneity, order/disorder, miscibility gap, and morphology of the sample.

2. Local geometry. The local crystal-chemical and structural properties evolve as a function of the concentration of an element in a solid-solution rock-forming mineral series and they are related to the thermodynamic properties and stability of the minerals. However, most of the experimental studies associated with these properties use macroscopic and thus heterogeneous samples, giving average values of these properties. The knowledge of these properties in a real local environment free of the order/disorder and average compositional effects is key to determine the micro- and even the nano-behaviour. Computational studies, at a high theoretic level, can yield precise information on this matter, offering a detailed explanation for the local crystal-chemical behaviour of the crystalline solutions (Geiger, 2008), which in many cases is not provided by the experimental techniques. Therefore, we continued the study of our series by examining the local geometry as a function of Na^*.

The <O-H> distance values were 2% higher than the experimental values and they were constant throughout the series. This could be because of: i) the dangling nature of these bonds in the structure; and ii) the hydrogen bonds that the H atoms form with the nearest oxygens (Mookherjee, 2001, Botella et al. 2004), which remain in average constants along the series. The average bond length between tetrahedral cations and their oxygens, <T-O>, were less 1% higher than the experimental values. In general, most of these distances are overestimated with respect to the experimental known data, which could come from the general known trend of the GGA method to overestimate the covalent bonds in molecules (Tran et al. 2007). The average distance increased as a function of Na*, in

agreement with the experimental behaviour of the end members of the series. $<Al^{3+} - O>$ distances calculated in the Oc-sheet were also close to the experimental value (deviation <1%), following the same trend as <T-O> as a function of Na*.

Owing to the ditrigonal symmetry of the cavities, two types of distances could be defined from the interlayer cations (*X*) to the basal oxygens: i) the distance to the farthest oxygens ($X\cdots O_{outer}$); and ii) the distance to the nearest oxygens ($X\cdots O_{inner}$). Our calculated $<K\cdots O_{outer}>$ and $<K\cdots O_{inner}>$ were overestimated (2%) and underestimated (3%), respectively, with regard to the highest experimental values (Table 1); however, the corresponding <Na···O> distances were both lower by 5% and 6%, respectively, compared to the experimental data. The behaviour of these distances with respect to Na^* was approximately linear, decreasing with increasing Na^*. The differences between the two distances, $\Delta<X\cdots O> = <X\cdots O>_{outer} - <X\cdots O>_{inner}$, as a function of Na^* are shown in Figure 3a. At increasing substitution, $\Delta<X\cdots O>$ and their slopes are larger in Na^+ than in K^+ cavities. These variations could be due to the fitting of the cavities to the Na^+ size, and, consequently, induce a lack of fitting in the K^+ neighbour cavities, introducing some stability/instability with respect to the different cavity type in the mineral. This effect could be related to the gap of miscibility at the middle concentration range of the series. In general, our values showed larger values than the experimental values (Fig. 3a).

Another way to study the interactions of the interlayer cations and the basal oxygens was the average tetrahedral rotations (<α>), which were overestimated for the Ms and Pg values, a small deviation appearing for the last samples (Fig. 3b, Table 1). The α angle of both Na^+ and K^+ ditrigonal cavities increased as a linear function of Na^* (Fig. 3b, Table 1), the values and slope of $<\alpha>_{Na}$ being higher than $<\alpha>_K$, indicating that the higher charge/radius ratio of Na^+ with respect to K^+ increased the tetrahedral rotation (Muñoz-Santiburcio et al. 2011), and the α angle would work as a hinge to open or close the tetrahedral cavities, depending on the cation inside. All this indicates that the variation of tetrahedral rotation in the K^+ cavities as a function of Na* could be induced by rotations of the neighbouring Na^+ cavities. Therefore, a better fitting between both T- and Oc-sheets occurred as the Na^+ substitution increased (GEA92). In addition, substitutions in the Oc-sheet resulted in a decreasing of α and therefore these Oc-substitutions would not be

373 favoured in higher Na-substituted members, which could explain the scarcity of Oc-
374 substituted Pg's.

375 The difference of radii of the substitution cations, the rotation of the polyhedra of
376 the host place in the crystal structure, and the subsequent possible induction of
377 stability/instability in the crystal structure, producing a the gap of miscibility, was also
378 found in the KNa-hollandite, in which the medium- and high-concentrate Na hollandites
379 were not found to be stable (Mookherjee et al. 2009b and Deng et al. 2010) or were found
380 under very special conditions, as in meteorites.

381 Volumes of the Si and Al^{3+} tetrahedrons were also close to the experimental values
382 (Table 1) and increased as a function of the Na^{*}. However, the Al^{3+} octahedrons showed an
383 opposite behaviour.

384 The Oc-, T-sheet, interlayer thickness, and layer volumes were also close to the
385 known experimental values, but the interlayer thickness was lower than the experimental
386 values, just noted in the $½csin\beta$ parameter analysis. However, the deviations were larger
387 than the $½csin\beta$ deviations, which were compensated for by the octahedral thickness
388 deviation which went in the opposite direction. The basal oxygen corrugation (Δz) showed
389 the largest deviations from the known experimental data. Most of them showed a general
390 declining trend with respect to increasing Na^{*}.
391
392 **Elastic-stiffness constants**

393 Table 2 shows several sets of previous experimental and computational ECs. The
394 geometrical setting of the crystal in Cartesian coordinates is $c \,||\, z$, and b in the yz plane.
395 Although all calculations were performed in the P1 group, the ECs showed monoclinic
396 symmetry (Nye, 1957).

397 The 13 non-zero independent ECs of the Ms-Pg series are sorted into five groups: i)
398 $C_{ii(i\leq3)}$ pure normal ECs; ii) $C_{ii(3<i\leq6)}$ pure shear ECs; iii) $C_{ij(i\neq j,\ \leq3)}$ mixed normal ECs; iv)
399 $C_{i5(i\leq3)}$ mixed normal-shear ECs; and v) mixed shear ECs, where C_{46} is the only non-zero
400 member by symmetry considerations (Nye, 1957).
401
402 *1. ECs of Ms.* In the first group of ECs two sets were distinguished:

i) The high values of C_{11} and C_{22} were due to the strong covalent and coordination bonding character of the layer throughout the *x*-*y* plane. These values were very similar (Table 2), indicating that the *xy* plane was almost isotropic, in agreement with the equal values determined by Aleksandrov and Ryzhova (1961). These ECs were slightly higher (1%) than those of Vaughan and Guggenheim (1986), and McNeil and Grimsditch (1993) (Fig. 4a). The low deviation of these ECs could come from the low deviation of the *a* and *b* axes with respect to the experimental values of GEA92. However, the deviations of our cell parameters with respect to those of Vaughan and Guggenheim (1986) were greater, despite that their sample showed more octahedral and interlayer substitutions than in our sample. This was not taken into account in our calculations, and could induce other crystal-physical and crystal-chemical effects. Besides, the temperature effect was not taken into account in our calculations. Our computational values showed a maximum deviation of 7% with respect to the model 1 (GGA, P = 0 GPa, $E-E_i=0$ eV) values of Militzer et al. (2011). These deviations could come from the different geometry, the plane-wave basis set and electronic approaches used in those calculations. Nonetheless, they used as reliable values those coming from the LDA approach and the experimental cell parameters.

ii) The C_{33} value was approximately 2.5-fold lower than those of C_{11} and C_{22} (Table 2). This low value of C_{33} could be due to the following factors: 1) the stacking of layers and the interlayer space introduced between them along the *c* axis; 2) the possibility of penetration of the cations in the ditrigonal cavity; 3) the attractive Coulomb forces between interlayer cations and layers; and 4) the repulsive forces between the basal oxygens on both sides of the interlayer space. The value of C_{33} of Ms deviated from the maximum experimental value by approximately 11%, but elastic properties of the calculated mineral were approximately the same as the natural mineral (Fig. 4b). Nonetheless, other higher values have been reported for the elastic modulus of Ms: 79.3 GPa (determined by the nanoindentation technique in the direction normal to the basal plane, Zhang et al. 2009,) and the highest value of 100.8 Gpa (Mavko et

al. 1998). However, if we match our $½csin\beta$ value with that of Vaughan and Guggenheim (1986), their parameter is shorter than ours, which could yield a higher value of C_{33}, although the variety of octahedral and interlayer cation substitutions of the sample used by Vaughan and Guggenheim (1986) and the temperature effect could have caused the lower value of C_{33}. In this sense, though, the intrinsic approaches at the DFT method used in this computational study should not be disregarded. On the other hand, White et al. (2009) showed reliable internal geometries by using the experimental crystal structure and optimizing the internal atomic geometry, as a consequence a pressure of ~ 1 GPa appeared in the cell. Millitzer et al. (2011) followed the same technique to compute their ECs. In our study, however, we established very accurate cell parameter values for Ms, when they were matched with the GEA92 values, and a pressure < 0.002 GPa was found in our cell. Therefore, the resulting differences in our EC values with respect to the experimental values might be explained in the inherent approaches of the DFT method used in this paper and the lack of substitution out of the interlayer cation substitutions.

In the pure shear ECs, C_{66} was the stiffest, with values very close to the experimental ones. C_{44} and C_{55} were lower than C_{66} and overestimated with respect to the Vaughan and Guggenheim's (1986) and Millitzer et al.'s (2011) values (Fig. 4c and d). The involvement of the *c* axis in the shears of C_{44} and C_{55} was possibly responsible for their higher values compared to experimental.

In the mixed-normal EC group, C_{12}, C_{13}, and C_{23}, our values were higher than the experimental values (Vaughan and Guggenheim 1986, and McNeil and Grimsditch 1993) (Fig. 4e). Nevertheless, the relationships between them (those of C_{i3} were approximately 1.7-fold lower than those of C_{12}) showed a trend quite similar to that of the experimental data. However, Collins et al. (1992) from calculation based on empirical potentials provided a value of C_{12} approximately 4-fold greater than the other two constants. The involvement of the *c* axis in our C_{13}, and C_{23} values should be the origin of the high values found.

The mixed normal-shear constants, $C_{i5\ (i\leq3)}$, were roughly comparable to the experimental values of Vaughan and Guggenheim (1986) (Fig. 4f). Meanwhile, C_{46} showed a negative value as the experimental value of Vaughan and Guggenheim (1986) (Fig. 4c).

In general, our crystal structure and ECs agreed with the range of experimental values in Ms, in symmetry, individual values, and relative values between them. However, some misfits are shown, although the elastic behaviour of our computational mineral was approximately the same as that of the experimental mineral.

2 Influence of the interlayer cation ordering on the ECs. Different configurations for the Al^{3+} substitutions in the tetrahedral sheet are possible. Millitzer et al. (2011) have demonstrated that ECs are not affected in a meaningful quantity for the different Al^{3+}/Si configurations of the tetrahedral sheets. However, the order/disorder effect of the ECs related to the interlayer cations have not yet been studied. We investigated this phenomenon in a simplified way by calculating the ECs in different cation configurations within the interlayer space.

The interlayer cation configuration used in our periodic cell models at Na^{*}= 0.25/0.75 included one Na^{+} or K^{+} in the sequence of K^{+}'s/Na^{+}'s. Therefore, the Na*=0.5 is the only member of our models which admits meaningful different interlayer cation configurations. In this sample, the Na^{+} and K^{+} were taken initially in an alternating configuration along the *b* axis (**c0**, Fig. 1a). From this model, three additional systems were designed: i) by duplicating the *b* axis of configuration **c0** (Fig. 1a), and modifying the order of the cations in the lowest interlayer space of the supercell by joining two cations of the same atomic number, leaving the upper interlayer space of the model unchanged, the **2bc1** configuration was established (Fig. 1b); ii) by duplicating the *a* axis and alternating the cations in the highest interlayer space, and leaving the lowest interlayer space of the model as before, the **2ac1** configuration was established (Fig. 1c); and iii) one interlayer space containing only Na^{+} atoms and the other only K^{+} atoms (Fig. 1d). This last configuration could be considered an interstratified mineral model, in which Ms and Pg are segregated into different layers.

Table 3 shows ECs of the **c0**, **2ac1**, **2bc1** and interstratified configuration. The crystal structure and internal geometry are completely optimized. The **c0** arrangement

494 showed the lowest Total Energy (TE) of the three configurations (**c0**, **2ac1**, **2bc1**). The cell
495 parameters of the three configurations showed very close data. For $\frac{1}{2}csin\beta$, these small
496 differences might give the quadratic functional trend, as found by GEA92. These
497 configurations had very similar ECs (the maximum difference being approximately 1 GPa)
498 with the exception of C_{33}, in which **c0** and **2bc1** show the lowest and the highest values,
499 respectively, with a difference of 4 GPa (5%). Nonetheless, the difference of TE between
500 the two configurations was small, and both of them could be present in the mineral, so that
501 C_{33} would increase its value in consequence. The bulk and shear moduli of the
502 polycrystalline aggregate did not show such an increase (Table 3). In any case, our
503 configurations changed only in one interlayer, so that if both interlayers had the same
504 configuration we could expect a still greater increase in C_{33}. Therefore, we could expect
505 that a configuration with alternated cations along the *b* axis and aggregated cations along
506 the *a* axis would present a lower C_{33}. The other ECs and the moduli should change in small
507 quantities. However, the interstratified configuration showed the lowest TE and larger
508 changes in the ECs. The lowest TE of this compound with respect to the other
509 configurations could be partially responsible for the lack of natural Ms' and Pg's with 0.38
510 <Na*< 0.85 (GEA92). The uniformity of tetrahedral rotation angle, α, on each surface
511 could also stabilize the structure, explaining the trend of both minerals to segregate in the
512 middle concentration range.
513
514 *3. ECs of the Ms-Pg series.* C_{11} follows an increasing trend with increasing Na* up to reach
515 Na*= 0.5, afterwards decreasing, where the Pg reaches a value lower than the Ms (Table 2,
516 Fig. 4a). C_{22} fluctuates in a 2 GPa range, the value for Pg being approximately equal to Ms.
517 Both ECs can be approximately described by Eq. 9, with symmetric mixing terms
518 $\Delta\left(\frac{V}{C_{ii}}\right)_{mix}$. Because of the negative and positive signs for V/C_{11} and V/C_{22}, the mixing
519 terms might be considered as a defect and an excess of V/EC, respectively (Fig. 4a). Both
520 ECs should not vary greatly along the series because of the stiff covalent bonds. However,
521 the geometry of the layer changed along the series because of the shifts in the tetrahedral
522 rotation induced by the interlayer cation substitution. The importance of the change in

523 geometry along the series was highlighted in the volume used in Eq. 9 to systematize the
524 behaviour throughout the series.

525 C_{33} increased as a function of Na^* (Fig. 4b), which is consistent with the higher ionic
526 potential of the increasing concentration of the smaller cations. In this representation the
527 value of Na*=0.5 is outside of a possible regular quadratic function fitting; possibly the
528 different values of α in the different Na^+ and K^+ cavities could yield the especially low
529 value. This EC also can be described by Eq. 9 (Fig. 4b), with values of the mixing term
530 due to a symmetric excess of V/C_{33}. The higher C_{33} value of Pg could be explained as
531 follows: i) Na cations possess a higher charge/radius than K^+, the Na^+ layer interactions
532 being the strongest; and ii) the two basal surfaces of Pg at both sides of the interlayer space
533 are the closest, so that in Pg the repulsive forces of both oxygen basal surfaces will be the
534 highest when the crystal undergoes a compressive strain along the *c* axis.

535 The elastic behaviour of C_{44} and C_{55} as a function of the Na^* followed approximately a
536 decreasing linear trend with Na* (Fig. 4c), associated with an ideal addition mixing
537 behaviour (Eq. 7). Similar behaviour was also observed with C_{46} (Fig. 4c). C_{66} showed
538 values within a narrow range (1.3 GPa), and its behaviour as a function of Na* was
539 increasing and approximately linear, taking into account the three first terms and the last
540 one. However, the point at $Na^* = 0.75$ showed a minimum (Fig. 5d). Nonetheless, C_{66} was
541 described by Eq. 9 without any mixing term.

542 The elastic behaviour of mixed normal ECs C_{12}, C_{13}, and C_{23} showed a regular decrease
543 from Ms to Pg (Fig. 4e). C_{13} fitted to an ideal addition crystalline solution law (Eq. 7), and
544 C_{12} and C_{23} showed the same behaviour with similar excess mixing terms (Fig. 4e).

545 C_{15} and C_{25} showed a decreasing trend with excess mixing terms (Eq. 7, Fig. 4f).
546 C_{35} showed a maximum at Na*= 0.5, and it was not able to be fitted by any simple
547 function.

548 Therefore, most of the ECs decreased as Na^* increased, with the exception of C_{33} and
549 C_{66}, which showed the opposite trend, and C_{11}, C_{22} and C_{35}, which acted irregularly. Both
550 Eq. 7 and 9 were fitted in different ECs. Most of the mixing terms were in excess, except
551 for C_{11}.

552 The bulk modulus of the polycrystalline aggregate of Ms showed larger values (68.4
553 GPa) than those of Vaughan et al. (1986) (Table 2). The last value came from the

554 application of the Voigt-Reuss-Hill approach to their ECs, but the composition of the
555 sample in that experiment showed many more cations in different concentrations than our
556 ideal sample. This and the heterogeneity of the sample could contribute to the elastic
557 properties and consequently to the calculated bulk modulus. Besides, in literature there are
558 many values for the bulk modulus for Ms and phengite micas (Table 4), from the lower
559 value of 52 GPa (Sekine et al., 1991), from shock wave experiments, to the higher value of
560 61.4 GPa (Faust and Knittle, 1994), from diamond anvil experiments with X Ray
561 diffraction. This dispersion of data (Table 4) could be attributed to the different samples,
562 heterogeneities, techniques, compositions and powdered or single-crystal samples. By
563 means of DFT calculations with pressure applied to a crytal with periodic conditions up
564 to 6 GPa, a value of 60.1 GPa was obtained (Ortega-Castro et al. 2010), close to the
565 value of Faust and Knittle. The present value for Ms coming from the application of the
566 Hashin-Schtrikman-Hill approaches to the DFT-ECs is out of the range of the known
567 values of bulk modulus of Ms, which could come from the ideal composition,
568 computational model, and physical approaches used in this work. Nonetheless, DFT
569 calculations were performed at 0 K, and the bulk modulus generally decreases at
570 increasing temperature. From Comodi et al. (2002) in Ms there was a $\left(\frac{\partial B_T}{\partial T}\right)_P$ = -0.0146
571 GPa/K between 298 and 873 K, which could be considered linear from 0 K, and it could
572 yield an estimate of B_0, at 298 K, of 64.0 GPa, closer to the experimental values than the
573 value at 0 K (Table 4). In Pg, $\left(\frac{\partial B_T}{\partial T}\right)_P$ = -0.0109 GPa/K (Comodi et al. 2002) could also
574 yield an estimate of 65.5 GPa, at room temperature, closer to the experimental values
575 (65.0 GPa ,Comodi et al. 1997, and 59.9 GPa Comodi et al. 2002) than the value of 0 K.
576 The effect of temperature softened the computational bulk modulus values and can aid
577 to explain the differences with the experimental values. Figures 4g showed the bulk
578 modulus of the polycrystalline compounds as a function of the Na^*, which behaved
579 irregularly, with a minimum at 0.5. This lower resistance to the pressure of the middle
580 concentration sample could bring these minerals to migrate towards richer K^+ or Na^+

minerals. This again could be a hint to understand the gap of miscibility in this series. Nonetheless, the order/disorder effects would increase the modulus value, but not to a large extent. The shear modulus of Ms was much closer (37.9 GPa) to the values of Vaughan and Guggenheim (35.3 GPa). Figures 4h showed the shear modulus as a function of the Na^*, which decreased regularly with increasing Na*. By DFT methods, a similar softening as a function of Na* was noted in phase-X [$(K,Na)_2Mg_2Si_2O_7$, Mookherjee et al. 2009a]. Therefore, polycrystalline samples of Ms-Pg and phase-X series richer in K^+ appeared to undergo the shear stress better than did the samples richer in Na^+.

From these data the sound velocities can be determined, where the compressional and shear velocities (m/s) (Karki et al. 2001) decreased as a function of Na^* (Fig. 5).

4. Discussion. In mafic, ultramafic and sedimentary rocks of subducted slabs, Na-K white micas are widespread. If the rocks are formed by a polycrystalline phase of the Ms-Pg series minerals, the members at the middle concentrations showed less resistance to the pressure and, depending on the mineral assemblage, the pressure and the temperature, these middle members could migrate to lower or higher Na* or segregate into interstratified minerals. All of these could contribute to cause the miscibility gap in the series. In addition, it is well known that Pg's show a very restricted stability P-T range in high-pressure and high-temperature experiments (Domanik et al. 1996). Particularly during the prograde metamorphism of metapelites and metarhyolites of subsuction zones, Pg breaks down at 2.0-2.5 GPa and 550-700ºC, forming kyanite and omphacite. Meanwhile, Ms and phengite show broad stability in the P-T compositional space. The nature of the mineral, the chemistry of the mineral assemblage, and the physical and chemical properties of the Pg minerals play an important role in the P-T existence range, but resistance to pressure should also be important in this solvus. Since the bulk modulus of the series was found to be higher at the Pg's, with temperature effect estimation, which should be more stable with respect to pressure in the rocks. However, event though the shear stress is not important at hydrostatic pressure, the layered structure and the weak forces between layers of these minerals could make that the lower shear and mixed ECs for Pg's be meaningful, thereby Pg's would be weaken at increasing pressure. Therefore, the differences in the shear and mixed ECs, the limited value of the Na^+ in the Ms' minerals, the tendency of the series to move to K-richer minerals, and the incorporation of the Mg^{2+} to the Oc sheet of phengites

612 bolster the stability of the members richer in K^+, and they became much more widespread
613 in different lithologies. Both the Ms and Pg members of the series could admit Mg^{2+}, Fe^{2+},
614 and Fe^{3+} substitutions in the Oc sheet, but the high distortion of the α angle in the Pg
615 samples should transform these "Oc-substituted-Pg's" into unstable minerals. Na-
616 substituted Ms' underwent the unstabilization better than in the case of K-substituted Pg's.
617 This unstabilization could also contribute Pg's to have their field of stability bounded in the
618 P-T compositional spaces.
619 On the other hand, if (001)-oriented aggregates could be found in shales and in schists,
620 the higher value of C_{33} in Pg's could make them more resistant to the direct pressure. In this
621 case, Pg's would increase the stability range in the P-T composition space, and the system
622 would possibly evolve to Na-richer-substituted members at high pressure. Nonetheless,
623 event though the shear stress is not important at hydrostatic pressure, the layered structure
624 and the weak forces between layers of these minerals could make that the lower shear and
625 mixed ECs weaken Pg's with respect to the Ms', setting a balance with the C_{33} effect. All of
626 this increases the anisotropy in shales and schists.
627 As with other phyllosilicates (e.g., talc, chlorite, and phase A) in subduction settings
628 (Mainprice and Ildefonse, 2009), this series is highly anisotropic for seismic P- and S-
629 waves. Despite its highly anisotropic character, compared to other phyllosilicates in
630 subduction settings, it is very unlikely that Pg would exert a strong influence on the
631 seismological properties of subduction, because of its low volume fraction and its limited
632 stability along the common P-T-path of subducted crust.
633 Because of the higher resistance of Ms'/phengites, and in certain mineral assemblages,
634 they are important to transport high amounts of volatiles to high P and T regions (Poli et al.
635 2002). At high pressures and over broad temperature intervals, Ms'/phengites can react to
636 K-hollandite, a key mineral in the subducted sediment. In this way, Ms'/phengites could be
637 one of the links in the K transport to K-hollandite, and the latter may move K from the
638 deepest part in the subduction slabs to the upper mantle wedge in transporting K as a
639 signature element (Mookjerhee et al. 2009b). All of this appears to agree with the depletion
640 of K^+ from the silicates on Earth to the core (Bukowinski, 1976; Lee and Jeanloz, 2003;
641 Murphy et al., 2003; Lee et al., 2004).
642

643 **Normal Strains**

644

645 Strains affect the bonds and the atomic groups according to their bonding. Therefore, if the
646 change in bond lengths and atomic group geometry are studied as a function of the strains,
647 a bonding picture inside the crystal would result. Cousins (1978a, 1978b, and 1981) and
648 Catti (1989) studied the inner elasticity, calculating the inner elastic-stiffness constants
649 associated with the atoms or atomic groups. In the present work, our aim was to establish a
650 landscape of the bonding by studying only the deformation of bonds or atomic groups from
651 the strained cells, according to Eqs. 2-4 after the optimisation of the internal atomic
652 coordinates.

653 Because of the layered structure, C_{33} showed the most important variation as a
654 function of Na*, and the normal stiffness along the *z* axis was the softest. Therefore, only
655 the most notable deformations and normal strains along the *z* axis were shown, with the
656 exception of the <α> angle variations.

657 Deformabilities as a function of Na^* are shown in Table 5. Tetrahedra rotated
658 according to the *xx* or *yy* strains in an effort to fit the T- and Oc-sheet when the cell was
659 strained, and <α>'s showed negative deformabilities (the value of <α> decreases from the
660 negative to positive ε_{xx} or ε_{yy} strain). The intercepts of the previous equations applied to K^+
661 cavities was the <α> deformability of Ms, and the deformability of the Na^+ cavities could
662 be considered as the deformability at the limit when Na* $\rightarrow$ 0. The tetrahedral rotations of
663 the Na^+ cavities were, in absolute value, more deformable than those of K^+'s and decrease
664 along the series (Table 5), which agrees with the greater slopes Δ(Na···O) and $<\alpha>_{Na}$ as a
665 function of Na* (Fig. 3). For ε_{zz} the <α> deformability behaviour was the opposite and
666 smaller than that of ε_{xx}- and ε_{yy}-strains (Table 5). When the strains were applied along the z
667 axis, where the weakest bond occurs, the <α> showed the lowest deformability.

668 The ε_{zz} strain induced linear deformations on <T – O> and $<^{VI}Al^{3+}$ - O> and their
669 deformabilities ranged from 0.02 to 0.1 (Table 5). The $<^{IV}Al\text{-}O_{basal/apical}>$ were more
670 deformable than the $<Si\text{-}O_{basal/apical}>$, and the $<T\text{-}O_{apical}>$ was less deformable than the
671 basal one. The deformability variation as a function of the Na^* showed different behaviour
672 (Table 5): while the $<T\text{-}O_{basal}>$ decreases with the increasing Na^*, the $<T\text{-}O_{apical}>$
673 increased. The $<^{VI}Al^{3+}$ - O> showed the lowest deformability of these bonds.

674 The ε_{zz} strains induced larger deformabilities at $<X^{+}\cdots O_{outer}>$ and $<X^{+}\cdots O_{inner}>$ than
675 the previous distance deformabilities, between 3- and 10-fold larger than the previous
676 deformabilities (Table 5). The Coulomb forces between the interlayer cations and the
677 oxygens in the tetrahedral cavities were revealed with these large deformabilities. In
678 general, the $<X^{+}\cdots O_{inner}>$ were greater than the $<X^{+}\cdots O_{outer}>$ deformabilities, which agreed
679 with their thermal expansion coefficients (Mookherjee et al. 2002, Catti et al. 1989). The
680 deformabilities decreased with increasing Na^{*}, and in the Na cavities did so with higher
681 slope than the K cavities.
682 T- and Oc-sheet thickness deformabilities registered values according to the <T-O>
683 deformability, increasing their values with Na^{*} (Table 5). However, the interlayer space
684 showed remarkable deformations, with slopes of around 2.6, indicating that the interlayer
685 space was a heavily deformable region, which showed strong thermal expansion
686 [Mookherjee et al. 2002 (phengite-$2M_1$), Catti et al. 1989 (muscovite)]. This means once
687 again that this was the weakest bonded region in the mineral. This easy deformation could
688 be related to the possibility of swelling in the phyllosilicates, in such a way that other
689 foreign molecules (such as water, polar molecules, etc.) could enter the interlayer space.
690 However, this mineral series does not swell in a detectable way, and if the Ms-Pg series
691 could deform its interlayer space to such a degree, we might expect larger deformabilities
692 in typical swelling phyllosilicates, such as smectites. Furthermore, the small deformability
693 of $<\alpha>$ as a function of ε_{zz} could be accounted for by the high deformability of the
694 interlayer space, where any deformation along *c* axis affected mainly the interlayer space,
695 and the layers did not undergo any meaningful deformation.
696
697 **CONCLUSIONS**
698
699 The calculated crystal structure, bond lengths, angles, and other geometrical parameters
700 were very close to the experimental range of values. The computational crystal chemistry
701 showed a similar behaviour to that of natural minerals, even though in nature a miscibility
702 gap appears, and therefore our series could be considered to be a general ideal series. The
703 importance of the crystal-chemistry behaviour on the anisotropy of the crystal is shown.
704 The differences of the geometrical features in the Na^{+} and K^{+} tetrahedral cavities could

induce an inertial behaviour to the octahedral substitution in the most Na-substituted members of the series, which agrees with the lack of octahedral substituted Pg samples.

Theoretical ECs agreed approximately with Ms values in the literature. The change of the ECs with the different interlayer cation configurations assayed in this work is small, with a maximum deviation of 5% from the lowest to the highest values. Some of them could be present in the mineral, where cation-aggregation regions could appear. However, the interstratified sample shows the higher EC values and the most stable total energy, and therefore a possible Ms and Pg segregation could be induced at the middle concentration member of the series. In general, the behaviour of ECs along the series appeared to have a decreasing stiffness with the increasing Na*, some of them showing linear behaviour. C_{33} and C_{66} increases with Na*. Most of them showed a deviation of the ideal crystalline-solution addition law, with mixing terms depending on the concentration, and in some of them the volume was an important variable to systematize the system. The bulk moduli of the polycrystalline aggregates showed small differences in the lowest and highest members of the series, with a minimum in the middle concentration member, but with an estimate of the bulk moduli at room temperature, the Pg turned out to be stiffer than Ms. So the geometrical features, the stiffness and the stabilities of the interstratified sample at the middle concentration range seem to justify the gap of miscibility in the series. The shear modulus showed a moderate decrease along the series. The lowest shear and mixed ECs of the Pg's could justify the low range of existence of these minerals in the P-T space. The P and S velocities decrease as a function of Na*.

Normal strains, $\varepsilon_{ii,}$ affected the bonds or other geometrical features of the structure according to their bonding. The strongest bonds showed the smallest deformabilities, these being less than one tenth of the ε_{ii}. Average distances between the basal oxygens and interlayer cations showed a high deformability in agreement with the weak interactions. The deformability of the interlayer space is the largest, according to its weakest bonding in the crystal structure. In general, deformabilities show linear functional behaviour with Na^*.

ACKNOWLEDGEMENTS

The authors thank to Profs. J. I. Soto, E. Puga, and C.J. Garrido-Marín for fruitful discussions, and wish to express their appreciation to the "Centro de Supercomputación de Galicia" (CESGA), and "Centro de Servicios de Informática y Redes de Comunicaciones (CSIRC), Universidad de Granada", for providing the computing time. This work is supported by Spanish MCINN and European FEDER grants CGL2005-02681 and CGL2008-02850/BTE, and TRA2009-0205, and the regional agency 'Junta de Andalucía' for the RNM-264 and -363 PAI-grants.

REFERENCES CITED

Adams, D.J., Oganov, A.R. (2006) Ab initio molecular dynamics study of CaSiO3 perovskite at P–T conditions of earth's lower mantle. Physical Review B 73, 184106.

Alexandrov, K. S., and Ryzhova, T. V. (1961) Elastic properties of rock-forming minerals. II Layered silicates, Bulletin Academy of Sciences USSR, Geophysics Series, English translation 12, 871-875.

Artacho, E., Sánchez-Portal, D., Ordejón, P., García, A., and Soler, J.M. (1999) Linear-scaling ab-initio calculations for large and complex systems. Physica Status Solidi (b), 215, 809–817.

Babuska, V., Fiala, J., Kumazawa, M., Ohno, I.Sumino, Y (1978) Elastic property of garnet solid-solution series. Physics of the Earth and Planetary Interiors, 16, 157 - 176

Blencoe, J. G., Guidotti C. V., and Sassi F.P (1994) The paragonite-muscovite solvus:II. Numerical geothermometers for natural, quasibinary paragonite-muscovite pairs. Geochimica et Cosmochimica Acta, 58, 2277-2288.

Botella, V., Timón, V., Escamilla-Roa, E., Hernández-Laguna, A., and Sainz-Díaz, C. I. (2004) Hydrogen bonding and vibrational properties of hydroxyl groups in the cristal lattice of dioctahedral clay minerals by means of first principle calculations. Physics and Chemistry of Minerals, 31, 475-486.

Brigatti, M.F., Frigieri, P., and Poppi, L. (1998) Crystal chemistry of Mg-, Fe-bearing muscovites-2M1. American Mineralogist, Volume 83, pages 775–785,

Bukowinski, M.S.T. (1976) Effect of pressure on physics and chemistry of potassium. Geophysics Research Letters 3, 491–494.

Burnham, C. W. and Radoslovich, E. W. (1964) Crystal structure of coexisting muscovite and paragonite. Carnegie Institute of Washington Year Book 63, 232-236.

Catti, M. (1989) Crystal elasticity and inner strain: a computational model, Acta Crystallographica, A45, 20-25.

Catti. M., Ferraris, G., and Ivaldi, G. (1989)Thermal strain analysis in the crystal structure of muscovite $2M_1$ at 700 ºC, European Journal of Mineralogy, 1, 625-632.

Catti M, Ferraris G, Hull S, and Pavese A (1994) Powder neutron diffraction study of 2M1 muscovite at room pressure and at 2 GPa, European Journal of Mineralogy, 6, 171-178.

Ceperley, D.M. and Alder, B.J. (1980) Ground state of the electron gas by a stochastic method. Physical Review Letters, 45, 566–569.

Collins, D.R., Richard, C., and Catlow, A. (1992) Computer simulation of structures and cohesive properties of micas. American Mineralogist, 77, 1172 - 1181.

Comodi, P. and Zanazzi, P.F. (1995) High-pressure structural study of muscovite. Physics and Chemistry of Minerals, 22, 170–177.

- (1997) Pressure dependence of structural parameters of paragonite. Physics and Chemistry of Minerals, 24, 274-280.

Comodi, P., Gatta, G.D., Zanazzi, P.F., Levy, D., and Crichton, W. (2002) Thermal equations of state of dioctahedral micas on the join muscovite-paragonite. Physics and Chemistry of Minerals, 29, 538–544.

Cousins, C. S. G. (1978a) Inner elasticity, Journal of Physics C. Solid State Physics, 11, 4867 – 4879. doi: 10.1088/0022-3719/1½4/017.

- (1978b) The symmetry of inner elastic constants, Journal of Physics C. Solid State Physics, 11, 4881 – 4900. doi: 10.1088/0022-3719/1½4/018.

- (1981) The corumdum structure: internal strain tensors and cluster configuration under stress. Journal of Physics C. Solid State Physics, 14, 1585 – 1602. doi: 10.1088/0022-3719/14/11/019.

Curetti, N., Levy, D., Pavese, A., and Ivaldi, G. (2006) Elastic properties and stability of coexisting 3T and 2M1 phengite polytipes. Physics and Chemistry of Minerals, 32, 670–678.

Cygan R.T., and Kubiki J.D. (2001) Molecular Modeling Theory: Applications in the Geosciences. In Reviews in Mineralogy and Geochemistry. Mineralogical Society of America, Chantilly, Virginia, USA. Vol. 42. ISSN 1529-6466.

Deng L. Liu X., Liu H., and Dong J. (2010) High-pressure phase relations in the composition of albite $NaAlSi_3O_8$ constrained by an abinitio and quasi-Harmonic Debye model, and their implications, Earth and Planetary Science Letters 298, 427-433.

Domanik, K., and Holloway, J., (1996) The stability and composition of phengitic muscovite and associated phases from 5.5 to 1 GPa: Implication for deeply subducted sediments. Geochimica et Cosmochimica Acta, 60, 4133-4150.

Eugster, H.P., Albee, A. L., Bence, A. E., Thompson, Jr, J. B., and Waldbaum, D. R. (1972) The two-phase region and excess of mixing properties of Paragonite-Muscovite crystalline solution. Journal of Petrology, 13, 147 – 179.

Faust, J. and Knittle, E. (1994) The equation of state, amorphization and high pressure phase diagram of muscovite. Journal of Geophysical Research, 99, 19785–19792.

Flux, S., Chatterjee, N. D. (1986) Experimental reversal of the Na-K exchange reaction between muscovite-paragonite crystalline solutions and a 2 molal aqueous (Na,K)Cl fluid. Journal of Petrology, 27, 665-676.

Gale JD, Rohl AL, Milman V, and Warren MC (2001) An ab initio study of the structure and properties of aluminium hydroxide: gibbsite and bayerite. Journal of Physical Chemistry B 105,10236–10242.

Geiger, Ch. A, (2008) Silicate Garnet: A micro to macroscopic (re)view. American Mineralogist, 93, 360 -372.

Guggenheim, S., Chang, Y.-H., and Koster van Groos, A. F. (1987) Muscovite dehydroxylation: High-temperature studies, 72, 537-550.

Guidotti C. V., Mazzoli C., Sassi F.P., and Blencoe, J. G. (1992) Compositional controls on the cell dimensions of $2M_1$ muscovite and paragonite. European Journal of Mineralogy, 4, 283 - 297.

- Sassi F.P., Blencoe, J. G., and Selverstone (1994) The paragonite-muscovite solvus:I. P-T-X limits derived from the Na-K compositions of natural, quasibinary paragonite-muscovite pairs. Geochimica et Cosmochimica Acta, 58, 2269-2275.

- Sassi, F. P. (1998) Petrogenetic significance of Na-K white micas mineralogy: recent advances for metamorphic rocks. European Journal of Mineralogy, 10, 815 - 854.

- Sassi F.P., Comodi P., Zanazzi P.F., and Blencoe J. (2000) The contrasting responses of muscovite and paragonite to increasing pressure: petrological implications. The Canadian Mineralogist, 38*,* 707 - 712.

Hashin Z, and Shtrikman S (1962a) On some variational principles in anisotropic and non-homogeneus elasticity, Journal of Mechanical Physics of Solids 10, 335 – 342.

- (1962b) A variational approach to the theory of the elastic behaviour of polycrystals, Journal of Mechanical Physics of Solids 10, 343 – 352.

Hill R. (1952) The elastic behaviour of a crystalline aggregate. Proceeding Physical Society of London A **65**, 349-354.

Hohenberg, P. and Kohn, W. (1964) Inhomogeneous electron gas. Physical Review B, 136, 864–871.

Iiyama, J. T., (1964) Étude des réactions d'éxhange d'ions Na-K dans la série Muscovite-paragonite. Bulletine de la Socité Française de Mineralogie et Crystallographie. LXXXVII, 532 - 541.

878 Isaak, D. G., and Graham, E. K., (1976) The elastic properties of an almandine-spessartine
879 garnet and elasticity in the garnet solution of the series. Journal of Geophysical Research,
880 81, 2483-2489.
881
882 Karki, B. B.; Stixrude, L.; Clark, S. J.; Warren, M. C.; Ackland, and G. J.; Crain, J. (1997a)
883 Structure and elasticity of MgO at high pressure, American Mineralogist, 82, 51-60.
884
885 - (1997b) Elastic properties of orthorhombic MgSiO3 perovskite at lower mantle
886 pressures, American Mineralogist, **82**, 635-638.
887
888 - Stixrude, L. and Wentzcovitch, R. M. (2001) High-pressure elastic properties of
889 major materials of Earth's mantle from first principles. Reviews in Geophysics, *39*,
890 507–534.
891
892 Knurr, R. A. and Bailey, S. W. (1986) Refinement of Mn-substituted muscovite and
893 phlogopite, Clays and Clay Minerals, 34, 7-16.
894
895 Kohn, W. and Sham, L.J. (1965) Self-consistent equations including exchange and
896 correlation effects. Physical Review, 140, A1133–A1138.
897
898 Lee, K.K.M., and Jeanloz, R. (2003) High-pressure alloying of potassium and iron:
899 radioactivity in the Earth's core? Geophysical Research Letters 30, 2212,
900 DOI:10.1029/2003GL018515.
901
902 - Steinle-Neumann, G., and Jeanloz, R. (2004) Ab-initio high-pressure alloying
903 of iron and potassium: implications for the Earth's core. Geophysical Research
904 Letters 31, L11603, DOI:10.1029/2004GL019839.
905
906 Lin, C. Y., and Bailey, S. W. (1984) The crystal Structure of Paragonite $2M_1$. American
907 Mineralogist, 69, 122 – 127.
908
909 McNeil, L. E., and Grimsditch, M. (1993) Elastic moduli of muscovite mica. Journal of
910 Physics: Condenser Matter, 5, 1681-1690.
911
912 Mainprice D. and Ildefonse B. (2009) Seismic Anisotropy of Subduction Zone Minerals–
913 Contribution of Hydrous Phases: Subduction Zone Geodynamics.S. Lallemand and F.
914 Funiciello (eds.). Springer-Verlag.Doi :10.1007/978-3-540-87974-9.
915
916 Mavko G., Mukerji, T., Dvorkin, J., 1998. The rock physics handbook. Cambridge
917 University Press, New York.
918
919 Mercier, P. H. J., Rancourt, D. G., Redhammer, G. J., Lalonde, A. E., Robert, J.-L.,
920 Berman, R. G., and Kodama, H. (2006) Upper limit of the tetrahedral rotation angle and
921 factors affecting octahedral flattening in synthetic and natural 1M polytype C2/m space
922 group micas. American Mineralogist 91, 831-849.
923

Militzer, B., Wenk, H.-R., Stackhouse S., and Stixrude L. (2011) First-principles calculation of the elastic moduli of sheet silicates and their application to shale anisotropy, American Mineralogist, 96, 125–137.

Milman V, and Winkler B (1999) Ab initio modeling in crystallography International Journal of Inorganic Matter, 1, 273 – 279.

- Warren, M. C. (2001) Elastic properties of TiB2 and MgB2, Journal of Physics: Condenser Matter, 13, 5585-5595.

Mondol, N. H., Jahren, J., Bjorlykke, and Brevik, I, (2008) Elastic properties of clay minerals, The Leading Edge, 27, 758 – 770.

Mookherjee, M., Redfern, S. A. T., and Zhang, M. (2001) Thermal response of structure and hydroxyl ion of phengite 2M1: an *in situ* neutron diffraction and FTIR study European Journal of Mineralogy, 13, 545-555.

- Redfern, S. A. T. (2002) A high-temperature Fourier transform infrared study of the interlayer and Si-O-stretching region in phengite-$2M_1$, Clay Minerals 37, 323-336.

- Steinle-Neuman, G. (2009a) Elasticity of phase-X at high pressure. Geophysical Research Letters, 36, L08307, doi: 10.1029/2009GL37782.

- Steinle-Neuman, G. (2009b) Detecting deeply subducted crust from the elascitity of hollandite. Earth and Planatary Science Letters, 288, 349-358.

Moore, D. M., Reynolds, R. C., JR, (1989) X-Ray diffraction and the identification and analysis of clay minerals. Oxford University Press.

Muñoz-Santiburcio, D., Ortega-Castro, J., Huertas, F. J. , and Hernández-Laguna, A. (2011) Influence of the exchangeable cation on the adsorption of 2-nitro-1-propanol on smectite surface models, Chemical Physics Letters 515, 49 – 55

Murphy, D.T., Collerson, K.D., and Kamber, B.S. (2002) Lamproites from Gaussberg, Antarctica: possible transition zone melts of Archaean subducted sediments. J. Petrol. 43, 981–1001.

Nye J. F. (1957) Physical properties of crystal. Oxford Science Publications.

Oganov A.R., Brodholt J.P., and Price G.D. (2001). The elastic constants of MgSiO3 perovskite at pressures and temperatures of the Earth's mantle. Nature 411, 934-937.

Ortega-Castro J., Hernández-Haro N., Hernández-Laguna A., and Sainz-Díaz C.I. (2008) DFT calculation of crystallographic properties dioctahedral 2:1 phyllosilicates. Clay Minerals 43, 351 – 361.

- J. Hernández-Haro, N., Muñoz-Santiburcio, D., Hernández-Laguna, A, and Sainz-Díaz, C.I. (2009) Crystal Structure and Hydroxyl group vibrational frequencies of phyllosilicates by DFT methods. Journal of Molecular Structure THEOCHEM, 912, 82 – 87, DOI:10.1016/j.theochem.2009.02.013.

- Hernández-Haro, N., Timón, V., Sainz-Diaz, C.I., and Hernández-Laguna, A. (2010) High-pressure behaviour of 2M1 Muscovite. American Mineralogist, 95, 249 – 259. DOI: 10.2138/am.2010.3035.

Pascal, M. L., Roux, J. (1985) K-Na exchange equilibria between muscovite-paragonite solid solution and hydrothermal chloride solutions. Mineralogical Magazine, 49, 515 – 521.

Peacock, S. M., Rushmer, T., and Thompson, A. B. (1994) Partial melting of subducting oceanic crust. Earth Planetary Science Letters, 1, 227-2.

Perdew, J.P., Burke, K., and Ernzerhof, M. (1996) Generalized gradient approximation made simple. Physical Review Letters, 77, 3865–3868.

Poli, S. and Schmidt, M. W. (2002) Petrology of subducted slabs. Annual Review of Earth and Planetary Sciences, 30, 207-235.

Rothbauer, R (1971) Untersuchung eines 2M1-muskovits mit neutronenstrahlen, Neues Jahrbuch für Mineralogie Monatshefte, 143-154.

Ruox, J. and Hovis, G. L. (1996) Thermodynamic mixing model for muscovite-paragonite solutions based on solutions calorimetric and phase equilibrium data. Journal of Petrology, 57, 1241-1254.

Sánchez-Portal, D., Ordejón, P., Artacho, E., and Soler, J.M. (1997) Density-functional method for very large systems with LCAO basis sets. International Journal of Quantum Chemistry, 65, 453–461.

Sekine, T., Rubin, A.M., and Ahrens, T.J. (1991) Shock wave equation of state of muscovite. Journal of Geophysical Research, 96, 19675–19680.

Shannon, R. D. (1976) Revised Effective Ionic Radii and Systematic Studies of Interatomic Distances in Halides and Chaleogenides, A32, 751 – 767.

Sidorenko, O. V., Zvyagin, B. B., and S. V. Soboleva (1977) Refinement of the crystal structure of $2M_1$ paragonite by the method of high-voltage electron diffraction, Soviet Physics Crystallography 22, 554 – 556.

Smyth, J. R., Jacobsen, S. D., Swope, R. J., Angel, R. J., Arlt, T., Domanik, K., and Holloway, R. (2000) Crustal structures and compressibilities of synthetic $2M_1$ and 3T phengite micas, European Journal of Mineralogy, 12, 955-963.

Soboleva, S. V., Sidorenko, O. V. and Zvyagin, B. B. (1977) Crystal structure of paragonite 1M. Soviet Physics, Crystallography, 22 , 291-293.

Soler, J. M., Artacho, E., Gale, J. D., García, A., Junquera, J., Ordejón, P., and Sánchez-Portal, D. (2002) The SIESTA method for ab-initio order-N materials simulation. *J. Phys.:* Condens. Matt. 14, 2745-2779.

Stixrude, L. (2002) Talc under compression: Spinodal instability, elasticity, and structure. Journal of Geophysical Research, 107, 2327, DOI: 10.1029/2001JB001684.

- Peacor, D.R. (2002) First-principles study of illite-smectite and implications for clay mineral systems. Nature, 420, 165–168.

Takahashi, T. and Liu, L. (1970) Compression of ferromagnesian garnets and the effect of solid solutions on the bulk modulus. Journal of Geophysical Research 75, 5757-5766.

Tran, F., Laskowski, R., Blaha, P., and Schwarz, K. (2007) Performance on molecules, surfaces, and solids of the Wu-Cohen GGA exchange-correlation energy functional, Physical Review B 75, 115131-1-14. DOI: 10.1103/PhysRevB.75.115131

Troullier, N. and Martins, J.L. (1991) Efficient pseudopotentials for plane-wave calculations. Physical Review B, 43, 1993–2006.

Vaughan, M. T., and Guggenheim, S. (1986) Elasticity of Muscovite and Its Relationship to Crystal Structure, Journal of Geophysics Research, 91, 4657-4664.

Waldbaum, D. R., and Thomson, J. B., Jr (1968) Mixing properties of sanidine crystalline solutions. II Calculation based volume data. American Mineralogist, 53, 2000- 2017.

Watt, J.P. (1979) Hashin-Shtrikman bounds on the effective elastic moduli of polycrystals with orthorhombic symmetry. Journal of Applied Physics, 50, 6290-6295. doi:10.1063/1.325768.

- (1980) Hashin-Shtrikman bounds on the effective elastic moduli of polycrystals with monoclinic symmetry. Journal of Applied Physics. 51,. 1520–1524.

- (1987) POLYXSTAL: a FORTRAN program to calculate average elastic properties of minerals from single-crystal elasticity data, Computers and Geosciences, 13, 441 – 462.

- Peselnick, L. (1980) Clarification of the Hashin-Shtrikman bounds on the effective elastic moduli of polycrystals with hexagonal, trigonal, and tetragonal symmetry. Journal of Applied Physics 51, 1525–1531.

Weirich, T. E. (2004) First-principles calculations as a tool for structure validation in electron crystallography Acta Crystallography. A60, 75 – 81. DOI:10.1107/S01087673030 25042.

White, C. E., Provis, J. L., Riley, D. P., Kearley, G. J., and van Deventer, J. S. J. (2009) What is the structure of Kaolinite? Reconciling Theory and Experiment, Journal of Physical Chemistry B, 113, 6756-6765.

Zhang, G. Wei, Z. and Ferrel, R.E. (2009) Elastic modulus and hardness of muscovite and rectorite determined by nanoindentation, Applied Clay Science 43, 271–281

Table 1. Calculated and experimental structural parameters of Ms-Pg series (lengths in Å, angles in degrees, and volumes in Å^3). $Na^*=Na^+/(Na^++K^+)$.

Sample	Experimental*	Experimental‡,	Na^*=0.0	0.25	0.5	0.75	1.0
a	5.174-5.226	5.128-5.135	5.187	5.176#	5.160	5.152#	5.123
b	8.976-9.074	8.898-8.906	9.006	8.994	8.975	8.932	8.895
c	19.875-20.097	19.287-19.384	20.148	19.917	19.653	19.378	19.113
α	90.0		90.0	90.0	90.0	90.0	90.0
β	95.59-95.84	94.35-94.6	95.44	95.55	95.55	94.08	94.02
γ	90.0		90.0	90.0	90.0	90.0	90.0
Volume	926-945.4	877.51-883.6	936.999	922.829	906.007	889.581	868.767
O-H	0.95		0.974	0.974	0.974	0.974	0.974
T-O	1.64	1.653	1.651, 1.757	1.649,1.758	1.675,1.761	1.653, 1.763	1.655, 1.766
M-O	1.927-1.94	1.908-2.221	1.934	1.922	1.931	1.920	1.926
M-OH	1.911	1.896	1.918	1.918	1.912	1.911	1.903
τ	111.0		111.4	110.3	111.1	109.9	110.6
K-O_{outer}	3.272-3.373	-	3.427	3.402	3.384	3.372	-
K-O_{inner}	2.832-2.934	-	2.759	2.721	2.680	2.624	-
Δ_K	0.426-0.509	-	0.668	0.681	0.704	0.748	-
Na-O_{outer}	-	3.370-3.374	-	3.438	3.407	3.352	3.357
Na-O_{inner}	-	2.624-2.642	-	2.680	2.618	2.514	2.474
Δ_{Na}	-	0.746-0.732	-	0.758	0.789	0.838	0.883
Tetrahedral rotation α_K, α_{Na}(°)	10.3 †-11.3	16,16.2 19	14.6	15.1, 15.8	15.5 , 16.7	16.5, 17.5	18.8
V. (Td) Si,Al (Å^3)		2.32	2.273, 2.774	2.274, 2.784	2.282, 2.794	2.283, 2.810	2.298, 2.824
V. (Oh) Al (Å^3)		9.10	9.386	9.361	9.345	9.339	9.283
Tetrahedral sheet thickness (Å)	2.262 †	2.243	2.277	2.265	2.271	2.248	2.237
Octahedral sheet thickness (Å)	2.083 †	2.078-2.085	2.093	2.090	2.089	2.115	2.144
Interlayer thickness (Å)	3.375 †	3.053-3.090	3.361	3.273	3.128	3.021	2.867
Volume Intralayer (Å^3)	309.3 †		310.5	308.2	307.1	304.2	301.5
Volume Interlayer (Å^3)	158.0 †		157.0	152.3	144.9	139.0	130.6
Basal oxygen corrugation Δz (Å)	0.239 †	0.23-0.226	0.282	0.305	0.305	0.279	0.261

* Burnham and Radoslovish (1964) $K_{0.66}Na_{0.34}Al_2(AlSi_3)O_{10}(OH)_2$; Rothbauer (1971) $K_{0.85}Na_{0.1}(Al_{1.81}Fe^{2+}_{0.14}Mg_{0.12})(Al_{0.9}Si_{3.1})O_{9.8}(OH)_2$; Guggenheim et al. (1987) $K_{0.93}Na_{0.08}(Al_{1.83}Fe_{0.16}Mg_{0.01})(Al_{0.90}Si_{3.10})O_{10}(OH)_{1.83}F_{0.17}$ and $K_{1.00}Na_{0.03}Ca_{0.01}(Al_{1.93}Fe_{0.01}Mn_{0.01})(Al_{0.91}Si_{3.09})O_{10}(OH)_{1.88}F_{0.12}$; Catti et al. (1989) $K_{0.86}Na_{0.11}(Al_{1.93}Fe_{0.07}Mg_{0.02})(Al_{0.92}Si_{3.08})O_{10}(OH)_2$; Catti et al. (1994) $K_{0.90}Na_{0.07}(Al_{1.63}Fe_{0.23}Mg_{0.16}Ti_{0.03})(Al_{0.80}Si_{3.20})O_{10}(OH)_2$; GET92; Brigatti et al. (1998) Different compositions; Mookherjee and Redfern (2002) $K_{0.95}Na_{0.05}(Al_{0.76}Fe_{0.14}Mg_{0.10})_2(Al_{0.75}Si_{3.25})O_{10}(OH_{1.96}F_{0.04})$

† Comodi and Zanazzi (1995) $K_{0.9}Na_{0.07}Ba_{0.01}\square_{0.02}(Al_{1.84}Ti_{0.04}Fe_{0.07}Mg_{0.04})(Al_{0.98}Si_{3.02})O_{10}(OH)_2$

‡ Comodi and Zanazzi (1997) $Na_{0.88}K_{0.10}Ca_{0.01}Ba_{0.01}(Al_{1.97}Ti_{0.007}Fe_{0.01}Mn_{0.006})Si_{3.01}Al_{0.99}O_{10}(OH)_2$: GEA92; Lin & Baley, (1984) $K_{0.042}Na_{0.916}Ca_{0.018}\square_{0.024}(Al_{1.990}Fe_{0.028}Mg_{0.013}Ti_{0.003})(Al_{1.061}Si_{2.939})O_{10}(OH)_2$

values are divided by 2.

V. (Td) means volume of the tetrahedral sheet, V. (Oh) is the volume of octahedral sheet; $\tau = O_{basal}$-T-O_{apical} bond angles ; Tetrahedral rotation α (°) = ½ $\Sigma_{i=1,6}$ [120° - (O_b-O_b-O_b)$_i$]/6; Tetrahedral sheet thickness (Å) = [(mean z coordinate of basal O) – (mean z coordinate of apical O)]csin ß; octahedral sheet thickness (Å) = [(mean z coordinate of "upper" O and OH in the

1088 octahedral sheet) – (mean z coordinate of "lower" O and OH in the octahedral sheet)]c sin ß, Δz (Å) = measure of distortion off
1089 coplanarity in *z* coordinate of the basal O atoms.
1090
1091
1092
1093

Table 2. Calculated and experimental elastic constants, Cij, (GPa) of the Ms-Pg series. Na*=$Na^+/(Na^+ + K^+)$

C_{ij}	Ms[a]	Ms[b]	Ms[c]	Ms[d]	Ms[e]	*Na* = 0.0*	*0.25*	*0.5*	*0.75*	*1.0*
11	178.0	181.0	176.5	172.7	228.7	178.9	179.8	180.1	178.7	177.0
22	178.0	178.4	179.5	166.7	232.7	178.2	177.1	178.0	176.3	178.3
33	54.9	58.6	60.9	54.8	65.6	67.9	75.9	74.8	97.6	112.4
44	12.2	16.5	15.0	14.2	16.3	22.6	19.2	14.3	11.8	8.4
55	12.2	19.5	13.1	17.2	17.3	27.0	25.6	23.9	23.1	21.4
66	67.8	72.0	70.7	67.6	76.2	67.5	67.9	68.1	67.9	68.8
23	14.5	21.2	23.0	17.4	22.4	34.3	31.3	28.1	23.9	19.1
13	14.5	25.6	20.0	20.1	25.0	38.8	36.2	32.6	30.1	25.6
12	15.2	48.8	47.7	48.8	98.4	65.1	63.4	61.7	56.7	54.4
15		-14.2	-1.2	-17.7	-1.9	-14.1	-13.5	-13.5	-16.3	-18.5
25		1.1	11.1	-1.7	6.9	0.7	-0.2	-2.5	-8.0	-13.2
35		1.0	-0.7	-3.3	1.7	-0.9	2.0	3.4	0.0	0.1
46		-5.2	0.7	-4.4	4.8	-0.7	-2.5	-5.9	-6.2	-9.2
B_{HSH}[f]		58.2[g]				68.4	69.2	66.8	69.2	68.8
G_{HSH}[f]		35.3[g]				37.5	37.1	34.6	35.0	32.6

(a) Aleksandrov and Ryzhova.(1961).
(b) Vaughan and Guggenheim (1986).
(c) McNeil and Grimsditch. (1993).
(d) Calculations from plane waves, GGA P=0, Model 1. Militzer et al. (2011).
(e) Calculations based on empirical potential (Collins et. al. 1992).
(f) Values from Hashin-Shtrikman-Hill equations. Hashin et al. (1962a, b), Watt and Peselnick (1980), Watt (1979,1980, 1987). Hill (1952).
(g) Values from Voigt-Reuss-Hill equations.

Table 3.- Elastic-stiffness constants (GPa) at different interlayer cation configurations at Na/(Na+K) = 0.5.

C_{ij}	**c0**	**2ac1**	**2bc1**	Interstr
11	180.1	179.7	180.0	175.0
22	178.0	176.9	178.0	172.7
33	74.8	76.1	79.2	87.1
44	14.1	14.6	14.6	11.6
55	23.9	23.5	23.3	23.0
66	68.1	67.7	67.9	65.9
23	28.1	27.7	27.6	28.9
13	32.6	32.8	32.1	34.3
12	61.7	61.1	61.2	56.5
15	-13.5	-13.7	-14.2	-17.6
25	-2.5	-2.7	-3.8	-7.8
35	3.4	2.9	2.6	-0.6
46	-5.9	-5.0	-5.4	-7.3
B_{HSH}	66.8	66.9	67.6	68.5
G_{HSH}	34.6	34.8	35.1	33.0
Total Energy (eV)	-53840.32390	-53840.21336	-53840.30269	-53840.66671
a (Å)	10.321	10.327	5.162	10.311
b (Å)	8.975	8.970	17.934	8.951
c (Å)	19.653	19.651	19.619	19.662
β (º)	95,55	95.26	95.28	94.55
Vol (Å^3)	1812.015	1812.696	1808.566	1808.960

Table 4.- Bulk modulus values for Muscovite from different experimental and computational studies.

Ref.	B0 (GPa)
Vaughgan et al. 1986	58.2[a]
Sekine et al.,1991	52[b]
Faust & Knittle , 1994	61.4[c]
Catti et al.,1994	56[d]
Comodi & Zanazzi, 1997	56[c]
Smyth et al. 2000, Phengite	57[c]
Comodi et al. 2002	57.0[c]
Curetti et al. 2006, Phengite	57.3[c]
Ortega-Castro et al. 2010	60.1[e]
This work	68.4[e] (64.0[*])

[(a)] Brillouin Scattering
[(b)] Shock wave
[(c)] X-Ray Diffraction
[(d)] Neutron Diffraction
[(e)] DFT
[(*)] An estimate of the bulk modulus at 298 K from Comodi et al. 2002.

Table 5.- Deformabilities as a linear function of the Na^*.

Molecular group	ε_{ii}	$D^i_{\varepsilon ii}$	slope
$<\alpha>_K$	*xx*	-5.06	2.06
$<\alpha>_{Na}$	*xx*	-5.20	1.78
$<\alpha>_K$	*yy*	-4.90	1.62
$<\alpha>_{Na}$	*yy*	-4.92	1.78
$<\alpha>_K$	*zz*	0.87	-0.78
$<\alpha>_{Na}$	*zz*	-0.11	-0.26
$<^{IV}Al\text{-}O_{basal}>$	*zz*	0.116	-0.054
$<Si\text{-}O_{basal}>$	*zz*	0.063	-0.040
$<^{IV}Al\text{-}O_{apical}>$	*zz*	0.074	0.036
$<Si\text{-}O_{apical}>$	*zz*	0.044	0.057
$<^{VI}Al\text{-}O>$	*zz*	0.024[a]	-
$<K\cdots O_{inner}>$	*zz*	0.833	-0.109
$<K\cdots O_{outer}>$	*zz*	0.729	-0.25
$<Na\cdots O_{inner}>$	*zz*	0.900[b]	0.27
$<Na\cdots O_{outer}>$	*zz*	0.338[b]	0.55
<Tetr. thickness>	*zz*	0.080	0.140
<Oct. thickness>	*zz*	0.205	0.129
<Interla. thickness>	*zz*	2.583[a]	-

[a] Deformability of Ms, no clear linear behaviour was shown as a function of Na^*.
[b] Deformability of Pg (regression was performed as a function of K^*).

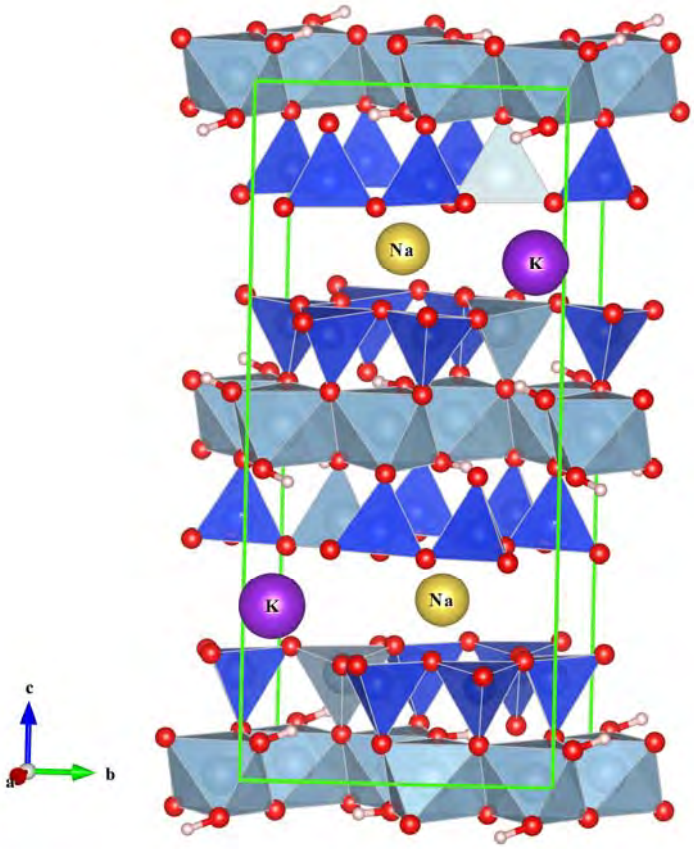

1128
1129 (a)

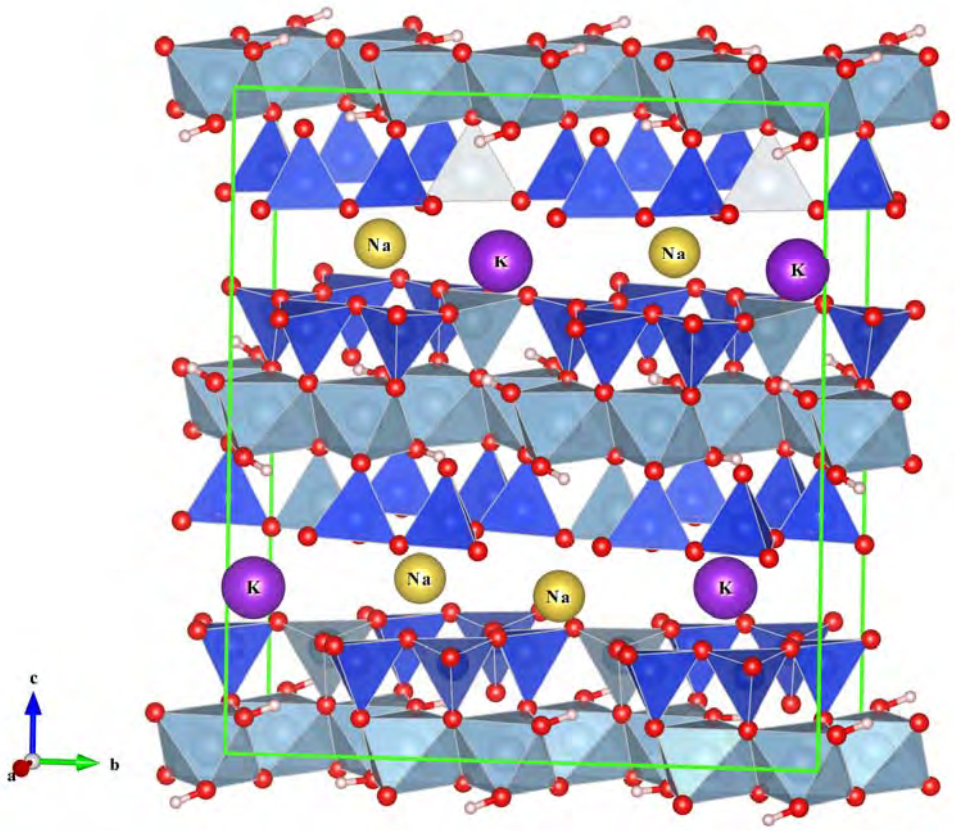

1130
1131 (b)

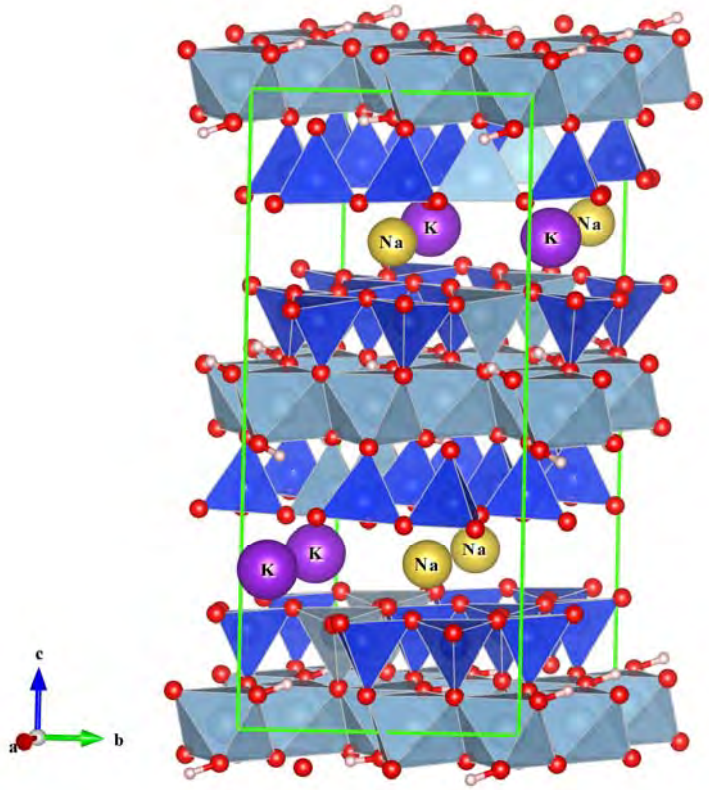

1132
1133 (c)

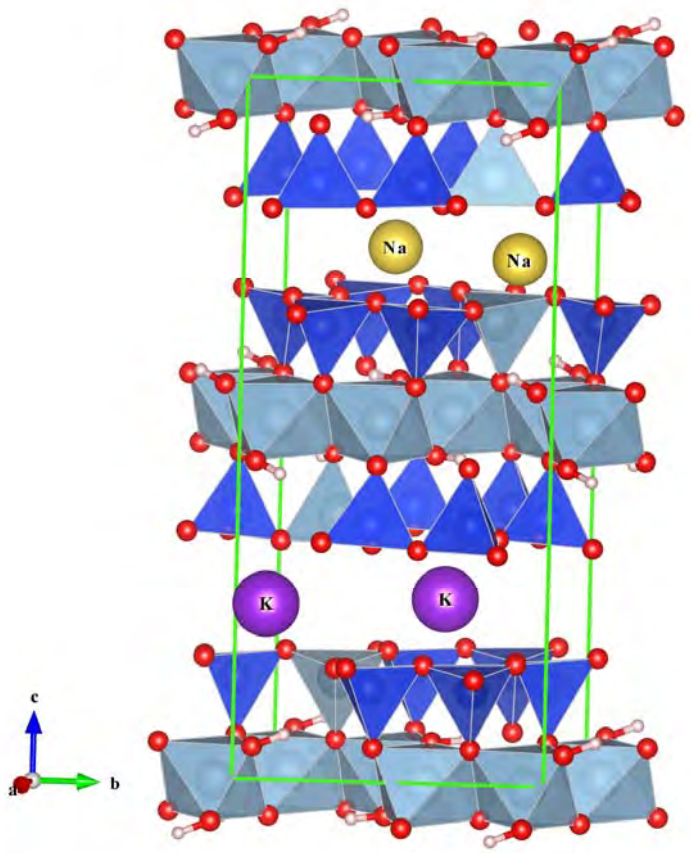

(d)

Figure 1. (a) Middle-concentration Na^{+} compound of the $2M_1$ Ms-Pg series, **c0** interlayer cation configuration; (b) **2bc1** interlayer cation configuration; (c) **2ac1** interlayer cation configuration; (d) interstratified derivative. Sky- and navy-blue polyhedra account for the Al^{3+} and Si^{4+} cation polyhedra, respectively; the O, H, Na, and K cation are represented by red, white, yellow, and purple spheres, respectively.

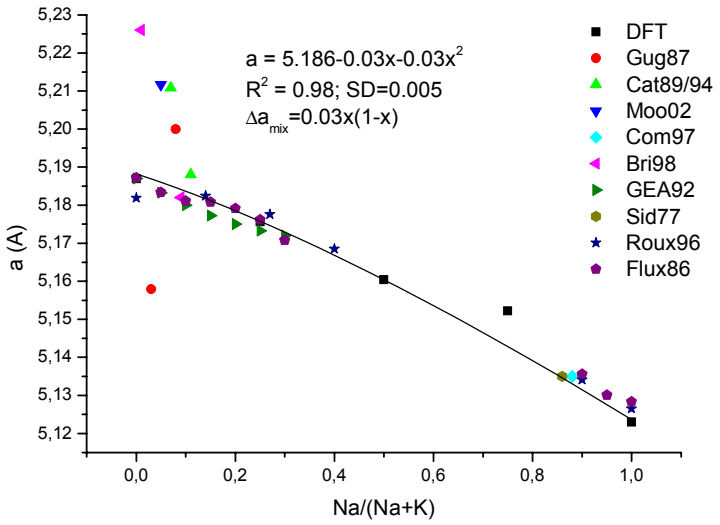

(*a*)

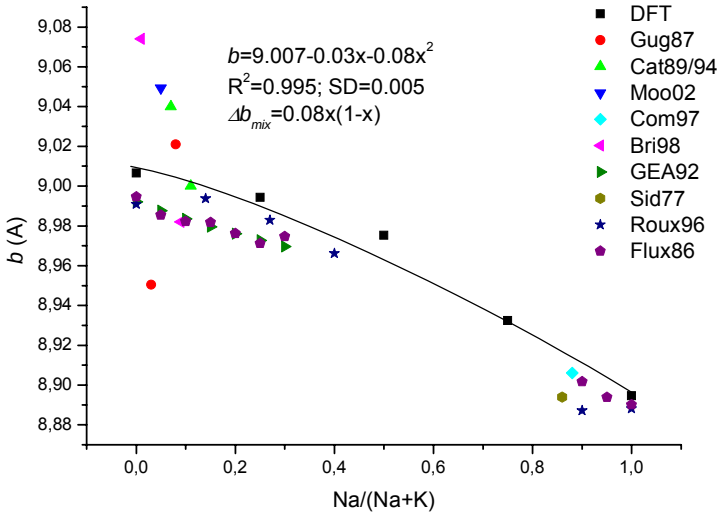

(*b*)

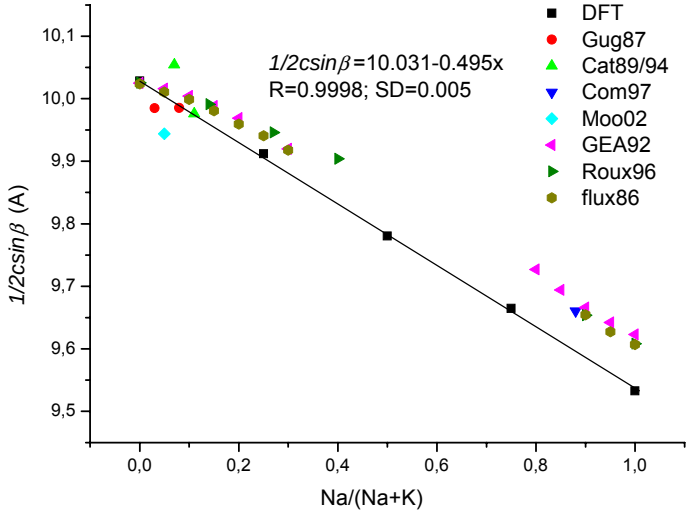

(*c*)

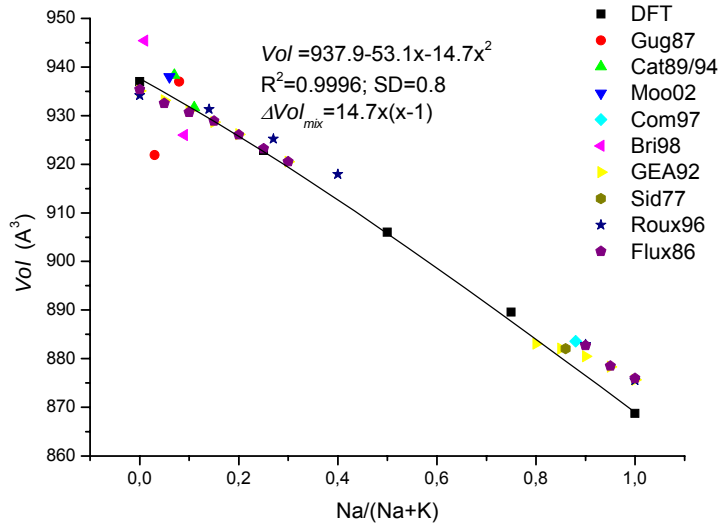

(*d*)

Figure 2. Computational and experimental values of (*a*) *a* axis; (*b*) *b* axis; (*c*) *½csinβ*; and (*d*) volume as a function of $Na^+/(Na^+ + K^+)$ in the Ms-Pg series. Inserts: linear least-square fitting, correlation coefficient (R) or square correlation coefficient, standard deviation (SD) and mixing terms; and experimental values extracted from different references. (*a*) and (*b*) GEA92 for *a* and *b* axes in the Ms region, values from Eqs. 2 and 8, respectively, of Table 1 from GEA92; (*c*) GEA92 in the Ms region values from Eq. 14 of Table 1, and in the Pg region values from Eq. 26 of Table 2 from GEA92; and (*d*) GEA92 in the Ms region values

1166 from Eq. 20 of Table 1, and in the Pg region values from Eq. 30 of Table 2 from GEA92.
1167 Sid77 = values from Sidorenko et al. (1977); Flux86 = values from Flux and Chatterjee
1168 (1986); Gug87= values from Guggenheim et al. (1987); Cat89/94 = values from Catti et al.
1169 (1989) and Catti et al. (1994); Roux96 = values from Roux and Hovis (1996); Bri98 =
1170 values from AG1 and/or RA1 and/or C3-29b samples from Brigatti et al. (1998); and
1171 Moo02 = values from Mookherjee and Redfern (2002).
1172

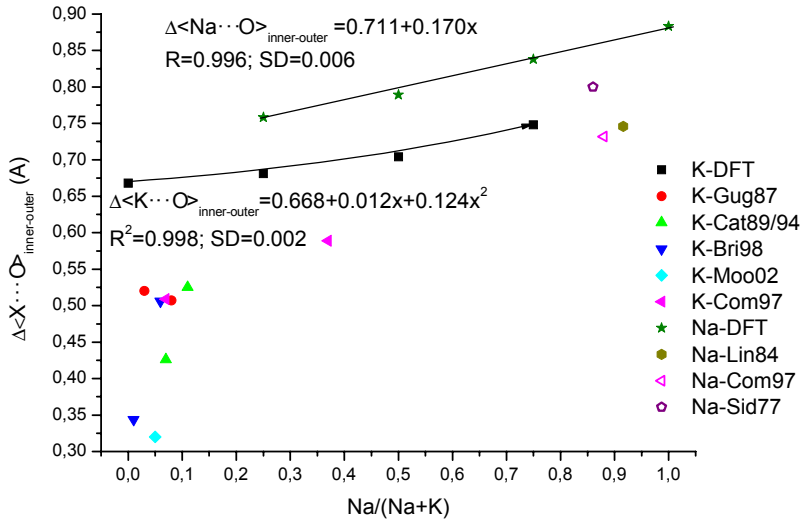

(*a*)

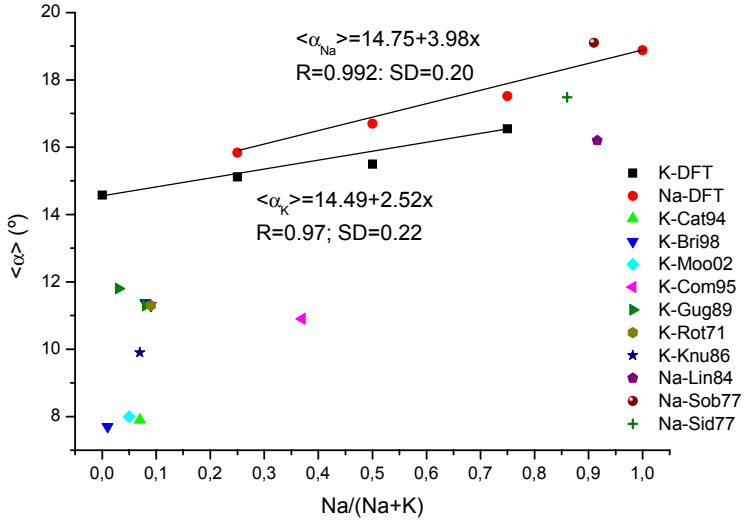

(*b*)

Figure 3.- (*a*) Differences between the $<X^{+}\cdots O>_{outer}$ and $<X^{+}\cdots O>_{inner}$ (Å) as a function of the $Na^{+}/(Na^{+}+K^{+})$; (*b*) average tetrahedral rotation (<α>) for the K^{+} and Na^{+} ditrigonal cavities as a function of the $Na^{+}/(Na^{+}+K^{+})$in the unit cell. Inserts: linear least-square fitting and experimental values extracted from different references. Rot71 = values from Rottbauer (1971); Sid77 = values from Sidorenko et al. 1977; Sob77 = values from Soboleva et al. (1977) (Pg 1M); Lin84 = values from Lin and Bailey (1984); Knu86 = values from Knurr and Bailey (1986); Gug87 = values from Guggenheim et al. (1987);

Cat89/94 = values from Catti et al. (1989) and (1994), respectively; Cat94= values from Catti et al. (1994); Com95 = values from Comodi et Zanazzi (1995); Bri89 = values from Brigatti et al. (1989); and Moo02 = values from Mookherjee and Redfern (2002).

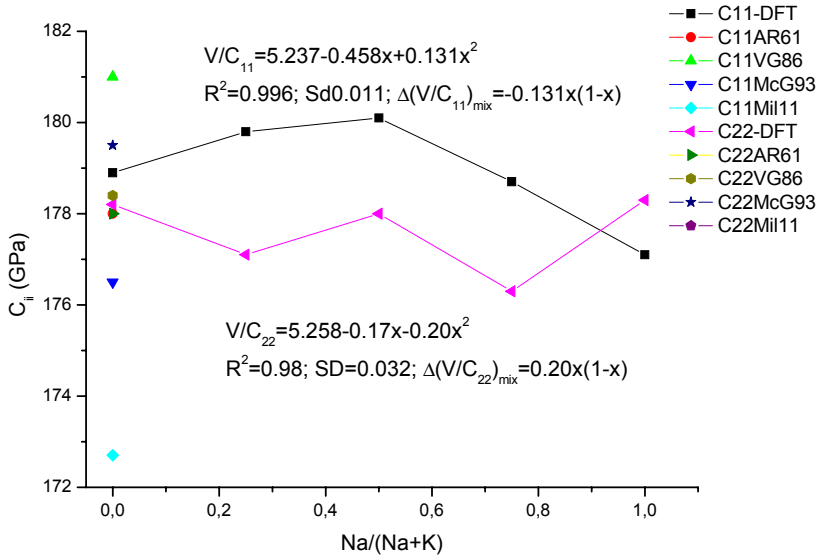

(*a*)

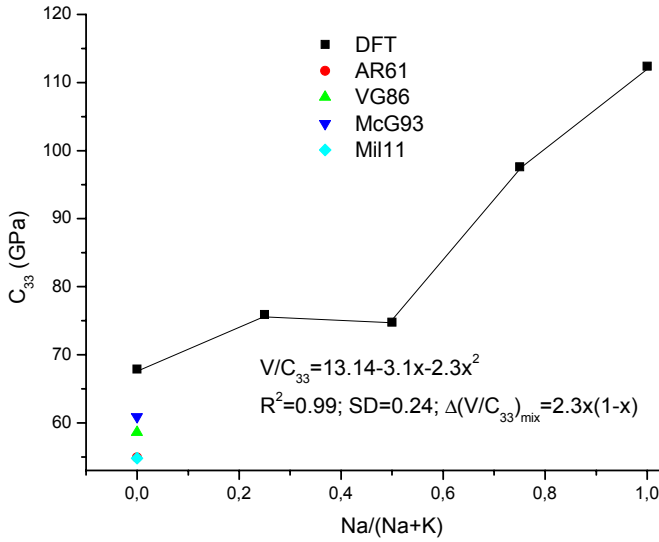

(*b*)

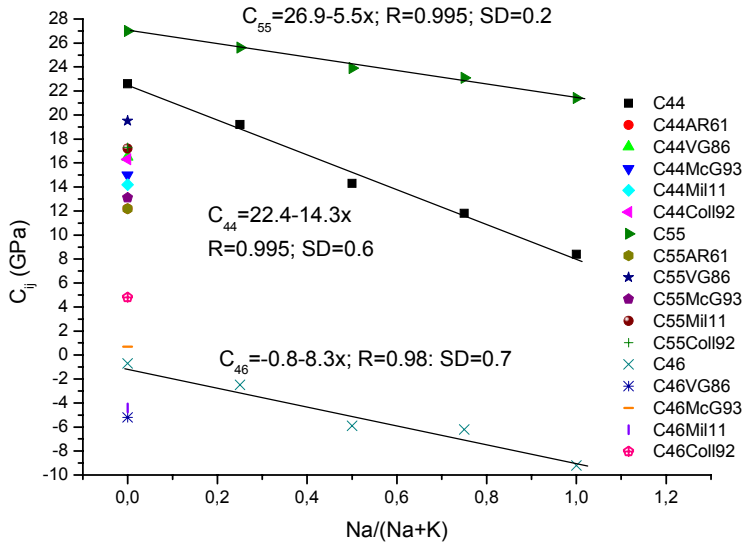

(*c*)

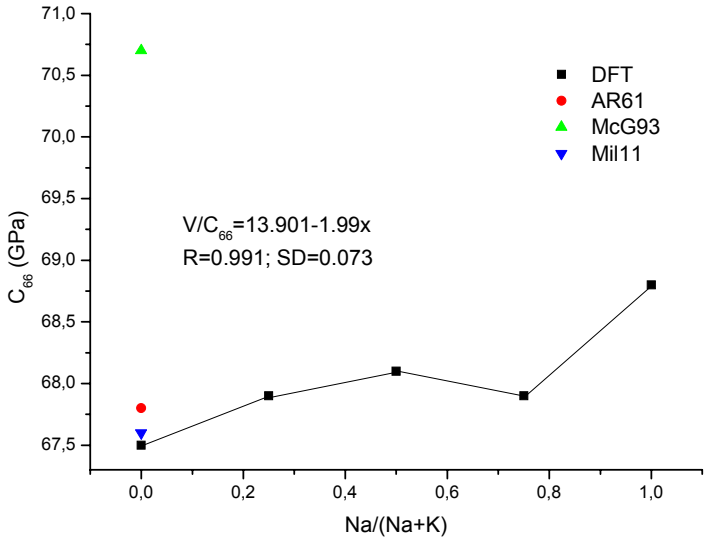

(*d*)

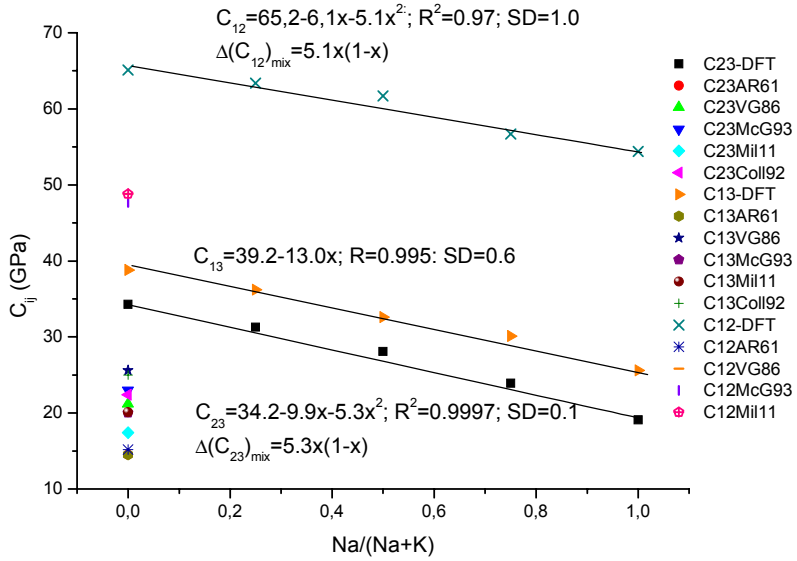

(*e*)

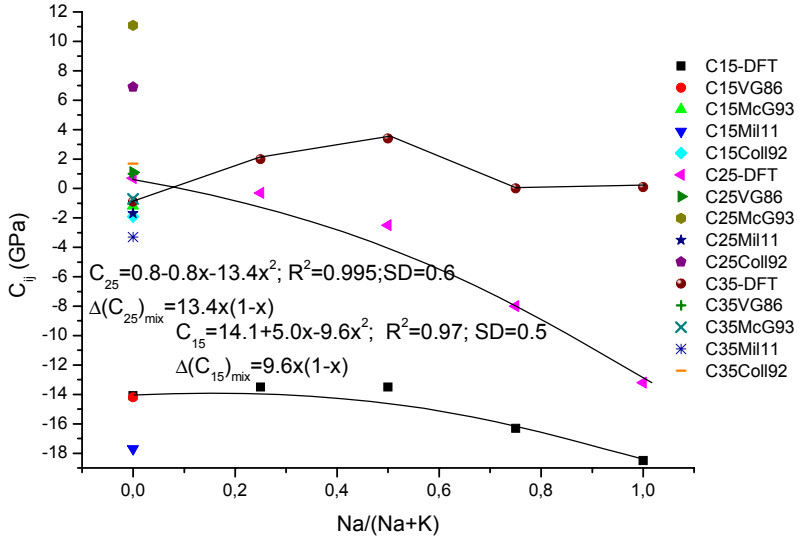

(*f*)

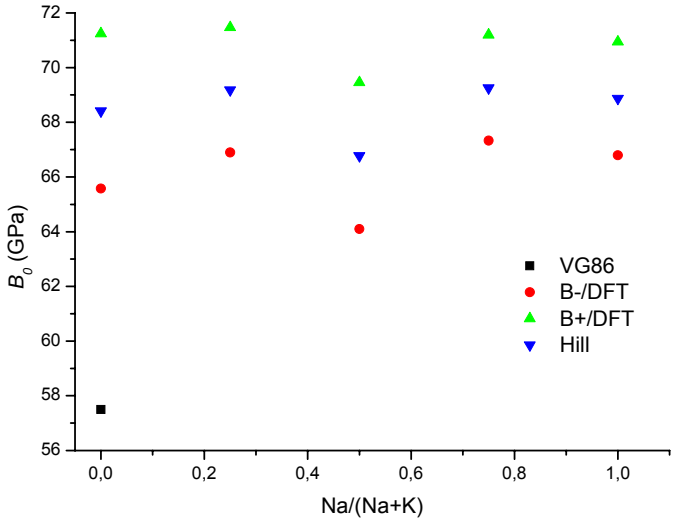

(*g*)

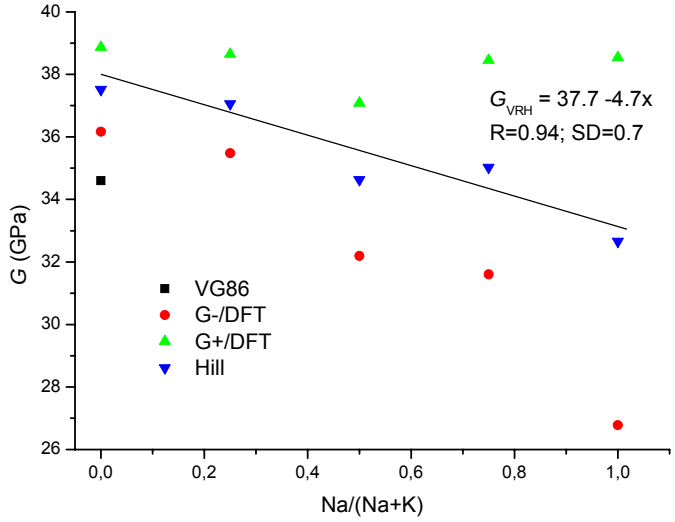

(*h*)

Figure 4.- C_{ij} (*a*) – (*f*), bulk (B) (*g*) and shear (G) (*h*) moduli as a function of $Na^+/(Na^+ + K^+)$. V/EC in $Å^3$/GPa. Inserts: linear least-square fitting and experimental values extracted from different references. In (*a*) – (*h*) AR61 = experimental values from Aleksandrov and Ryzhova (1961); VG86 = values from Vaughan and Guggenheim (1986); McG93 = values from McNeil and Grimsditch (1993); Mil11 = values from Militzer et al. (2011); Coll92 = values from Collins et al. (1992). In (*g*) and (*h*) B- and G- (B+ and G+) means Hashin-Shtrikman lower bound (upper bound) of the bull and shear moduli; Hill

means Hashin-Shtrikman-Hill average; VG86 means bulk and shear Voigt-Reuss-Hill average, respectively, from Vaughan and Guggenheim (1986).

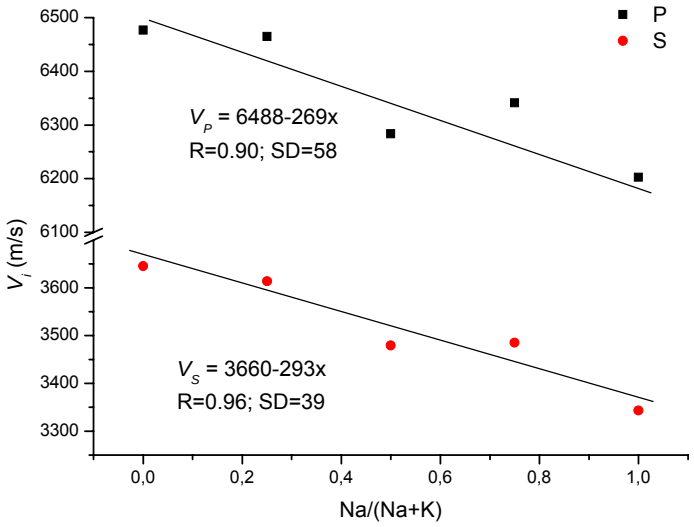

Figure 5.- P and S wave velocities (Karki et al., 2001) from the Hashin-Shtrikman-Hill modulis.